Article

SOURCE DATA TRANSPARENT PROCESS OPEN ACCESS CHECK FOR UPDATES

EMBO reports

SOX10 mediates glioblastoma cell-state plasticity

Ka-Hou Man[1,2,8], Yonghe Wu[3,4,8], Zhenjiang Gao[3], Anna-Sophie Spreng[1], Johanna Keding[5], Jasmin Mangei[1], Pavle Boskovic[1], Jan-Philipp Mallm[6], Hai-Kun Liu[3,4,7], Charles D Imbusch[5], Peter Lichter[1] & Bernhard Radlwimmer[1]✉

Abstract

Phenotypic plasticity is a cause of glioblastoma therapy failure. We previously showed that suppressing the oligodendrocyte-lineage regulator SOX10 promotes glioblastoma progression. Here, we analyze SOX10-mediated phenotypic plasticity and exploit it for glioblastoma therapy design. We show that low SOX10 expression is linked to neural stem-cell (NSC)-like glioblastoma cell states and is a consequence of temozolomide treatment in animal and cell line models. Single-cell transcriptome profiling of Sox10-KD tumors indicates that Sox10 suppression is sufficient to induce tumor progression to an aggressive NSC/developmental-like phenotype, including a quiescent NSC-like cell population. The quiescent NSC state is induced by temozolomide and Sox10-KD and reduced by Notch pathway inhibition in cell line models. Combination treatment using Notch and HDAC/PI3K inhibitors extends the survival of mice carrying Sox10-KD tumors, validating our experimental therapy approach. In summary, SOX10 suppression mediates glioblastoma progression through NSC/developmental cell-state transition, including the induction of a targetable quiescent NSC state. This work provides a rationale for the design of tumor therapies based on single-cell phenotypic plasticity analysis.

Keywords Glioblastoma; Phenotypic Plasticity; Therapy Resistance; Tumor Cell Quiescence; *SOX10*
Subject Categories Cancer; Stem Cells & Regenerative Medicine
https://doi.org/10.1038/s44319-024-00258-8
Received 4 February 2024; Revised 28 August 2024;
Accepted 4 September 2024
Published online: 16 September 2024

Introduction

Phenotypic plasticity refers to tumor cells' flexible adaptation to external perturbation primarily through non-genetic mechanisms. In the context of cancer treatment, it enables cell-state transition under therapeutic pressure, consequentially driving therapy resistance, escape, and ultimately tumor recurrence. It has emerged as one of the driving mechanisms of therapy resistance in many cancers (Chan et al, 2022; Hanahan, 2022; Tsoi et al, 2018).

Glioblastoma, the most common and aggressive adult brain tumor, is a prime example illustrating tumor phenotypic plasticity and its relationship with treatment failure (De Silva et al, 2023; Gimple et al, 2022; Yabo et al, 2022). Despite aggressive multimodal treatment strategies comprising maximal surgical resection and radio-chemotherapy using temozolomide (TMZ), glioblastoma patients typically succumb to the disease within 15 months due to rapid tumor recurrence (Stupp et al, 2005). Treatment failure in glioblastoma is primarily attributed to its extensive phenotypic plasticity that enables tumor cells to withstand the differentiation signals in the brain microenvironment (Brooks et al, 2021), immune surveillance (Gangoso et al, 2021; Liau et al, 2017), and anti-tumor therapy (Liau et al, 2017). Recent glioblastoma RNA sequencing (scRNA-seq) analyses revealed various tumor cell states co-existing along phenotypic gradients spanning states of aberrant neural development, mesenchymal-injury response and metabolic adaptation (Bhaduri et al, 2020; Couturier et al, 2020; Garofano et al, 2021; Neftel et al, 2019; Richards et al, 2021). These plasticity landscapes represent the molecular space in which cancer cells evade therapy by transitioning to resistant cellular states (Chen et al, 2012; Liau et al, 2017; Xie et al, 2022). To develop treatments that block these transitions and direct tumor cells to more manageable states, improving our understanding of the causes and phenotypic consequences of glioblastoma cell-state transitions in disease-relevant models will be essential.

Tumor progression is frequently mediated through co-opting differentiation factors that are critical during normal development (Al-Mayhani et al, 2019; Mu et al, 2017; Suva et al, 2014). Recently, we identified *SOX10* (SRY-Box Transcription Factor 10), which specifies oligodendrocytic lineage differentiation during normal NSC development (Stolt et al, 2002), as a master regulator of the RTK1-subtype of glioblastoma, and demonstrated that *SOX10* suppression promotes tumor progression (Wu et al, 2020). In line with these observations, low *SOX10* expression was reported to be associated with more aggressive and therapy-resistant phenotypes of melanoma (Capparelli et al, 2022; Sun et al, 2014).

Here, we used scRNA-seq analysis to map *SOX10*-dependent cell states in a syngeneic mouse glioblastoma model that reflects essential aspects of therapy-associated human tumor progression, including the emergence of a quiescent stem cell state. Pharmacologic targeting of these stem cells strikingly transformed the cell-state landscape and significantly extended animal survival.

---

[1]Division of Molecular Genetics, German Cancer Research Center (DKFZ), Heidelberg, Germany. [2]Faculty of Biosciences, Heidelberg University, 69120 Heidelberg, Germany. [3]Shanghai Institute for Advanced Immunochemical Studies, ShanghaiTech University, Shanghai, China. [4]Shanghai Clinical Research and Trial Center, 201210 Shanghai, China. [5]Division of Applied Bioinformatics, German Cancer Research Center (DKFZ), Heidelberg, Germany. [6]Single-Cell Open Lab, German Cancer Research Center (DKFZ), Heidelberg, Germany. [7]Division of Molecular Neurogenetics, German Cancer Research Center (DKFZ), Heidelberg, Germany. [8]These authors contributed equally: Ka-Hou Man, Yonghe Wu. ✉E-mail: b.radlwimmer@dkfz.de

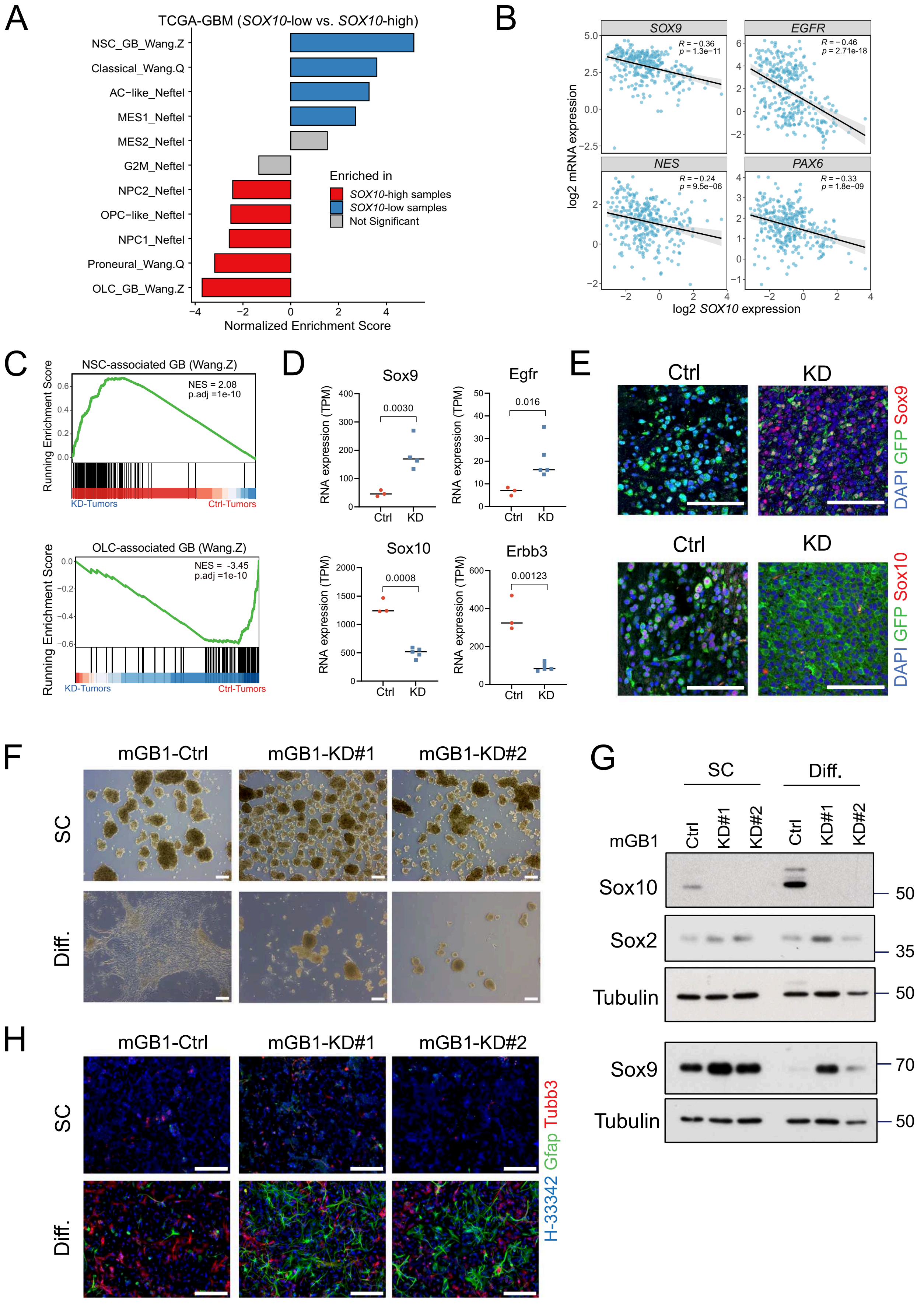
A
TCGA-GBM (SOX10-low vs. SOX10-high)
NSC_GB_Wang.Z
Classical_Wang.Q
AC−like_Neftel
MES1_Neftel
MES2_Neftel
G2M_Neftel
NPC2_Neftel
OPC−like_Neftel
NPC1_Neftel
Proneural_Wang.Q
OLC_GB_Wang.Z
−4 −2 0 2 4
Normalized Enrichment Score
Enriched in
SOX10-high samples
SOX10-low samples
Not Significant
B
SOX9
R = −0.36
p = 1.3e−11
EGFR
R = −0.46
p = 2.71e−18
NES
R = −0.24
p = 9.5e−06
PAX6
R = −0.33
p = 1.8e−09
log2 mRNA expression
log2 SOX10 expression
C
NSC-associated GB (Wang.Z)
NES = 2.08
p.adj =1e-10
Running Enrichment Score
KD-Tumors
Ctrl-Tumors
OLC-associated GB (Wang.Z)
NES = -3.45
p.adj =1e-10
KD-Tumors
Ctrl-Tumors
D
Sox9
0.0030
Egfr
0.016
Sox10
0.0008
Erbb3
0.00123
RNA expression (TPM)
Ctrl
KD
E
Ctrl
KD
DAPI GFP Sox9
DAPI GFP Sox10
F
mGB1-Ctrl
mGB1-KD#1
mGB1-KD#2
SC
Diff.
G
SC
Diff.
mGB1
Ctrl
KD#1
KD#2
Ctrl
KD#1
KD#2
Sox10
Sox2
Tubulin
Sox9
Tubulin
50
35
50
70
50
H
mGB1-Ctrl
mGB1-KD#1
mGB1-KD#2
SC
Diff.
H-33342 Gfap Tubb3

◀ **Figure 1. *SOX10*-high and *SOX10*-low samples occupy distinct glioblastoma cell states.**

(**A**) Bar plots summarizing the results of gene set enrichment analyses (GSEA) of the indicated genesets curated from several studies. In total, 324 glioblastoma IDH-WT samples of the TCGA cohort were stratified by *SOX10* expression and pre-ranked by log fold change. Differentially expressed genes between the top and bottom 25% of the samples were analyzed by GSEA. (**B**) Correlation between the expression of *SOX10* with other NSC/AC-like markers in the TCGA-GBM cohort. Pearson correlation tests were used to compute *R* and *P* values. (**C**) GSEA plots showing enrichment of neural stem cell (NSC)-associated and oligodendrocyte-lineage cell (OLC)-associated glioblastoma gene signatures in mGB1 *Sox10*-KD ($n = 5$) and control ($n = 3$) tumors, respectively. NES Normalized Enrichment Score, *P*.adj adjusted *P* value. Adjusted *P* values (*P*.adj) were calculated using the Benjamini–Hochberg method. (**D**) RNA Expression (transcripts per kilobase million; TPM) of NSC-associated genes *Sox9* and *Egfr* (top row) and OLC-associated genes *Sox10* and *Erbb3* (bottom row). Mean TPM expression values from control ($n = 3$ animals) and KD ($n = 5$ animals) were shown. Adjusted *P* values between expression levels from mGB1 *Sox10*-KD and control tumors were calculated with the standard 'limma' differential expression analysis. (**E**) Immunofluorescence images of Sox9 (NSC) and Sox10 (OLC) markers in mGB1 *Sox10*-KD and control mice. Scale bar = 100 µm. (**F**) Bright-field images of mGB1 control and *Sox10*-KD cells (KD#1 and KD#2) cultured in stem cell (SC) condition (top) or 10% fetal bovine serum (Diff.) for 7 days to induce differentiation (bottom). Scale bars = 200 µm. (**G**) Western blot analysis of the protein expression of Sox2 in mGB1 control and *Sox10*-KD cells cultured under SC or Diff. conditions. Tubulin was used as the loading control. (**H**) Immunofluorescence images of Gfap and β3Tubulin (Tubb3) in mGB1 control and Sox10-KD cells (KD#1 and KD#2) seeded in laminin-coated plates under SC (top) or Diff. (bottom) condition. Scale bars = 200 µm. Source data are available online for this figure.

Results

SOX10 expression correlates with glioblastoma cell state

Given the role of *SOX10* in the differentiation of neural stem and progenitor cells, we hypothesized that *SOX10* is a key factor determining glioblastoma cell state. Therefore, we analyzed the correlation of *SOX10* expression levels and glioblastoma cell state in 324 primary IDH-WT glioblastoma of the TCGA-GBM dataset. Gene set enrichment analysis (GSEA) using published genesets (Neftel et al, 2019; Wang et al, 2017; Wang et al, 2020) revealed that, consistent with the role of *SOX10* as a pivotal transcription factor of oligodendroglial development, proneural/oligodendrocyte-lineage cell (OLC)-related cellular states were significantly enriched in *SOX10*-high tumors, defined as samples with top quartile expression of *SOX10*. In contrast, neural stem cell (NSC)-related, classical, and astrocyte (AC)-like cell states were enriched in *SOX10*-low tumors (Fig. 1A). In line with these findings, *SOX10* expression was significantly anti-correlated with *SOX9*, *EGFR*, *NES*, and *PAX6* (Fig. 1B), suggesting that *SOX10*-high and *SOX10*-low tumor cells exhibit disparate lineage propensity, with *SOX10*-low tumor cells occupying an AC-like or NSC-like cellular state characterized by high *SOX9* and *EGFR* expression (Cancer Genome Atlas Research, 2008; Neftel et al, 2019; Verhaak et al, 2010).

SOX10 expression was proposed to be suppressed by therapy-related factors, i.e., radiation treatment in a glioblastoma mouse model (Lau et al, 2015), TGF-β-mediated stress signaling activated by irradiation, hypoxia, or TMZ in human glioma cells (Tabatabai et al, 2006), and BRAF inhibition in melanoma patients (Capparelli et al, 2022; Sun et al, 2014). We confirmed TMZ-induced *SOX10* suppression in the human glioblastoma cell lines cultivated in 2D-adherent culture or in co-culture with iPSC-derived cerebral organoids (Fig. EV1A,B). Western blotting analysis indicated robust expression of the DNA-repair protein O-6-Methylguanine-DNA Methyltransferase (MGMT) in NCH644 but not NCH421k or NCH441 cells (Fig. EV1C), consistent with previously reported TMZ IC50 values: NCH644, 227 mM; NCH421k, 272 µM; (Dirkse et al, 2019). In addition, TMZ-dependent Sox10 downregulation also was observed in a glioblastoma animal model (Rusu et al, 2019) (Fig. EV1D). These findings suggest that the effect of TMZ on SOX10 expression is likely independent of MGMT repair activity and might be mediated by TMZ-induced stress signaling as previously suggested (Tabatabai et al, 2006).

To test whether *SOX10* repression is sufficient to induce OLC-like to NSC-like cell-state transitions, we turned to a syngeneic mouse glioblastoma model, wherein *Sox10*-high mouse glioblastoma (mGB1) neurospheres were transplanted in immunocompetent mice. This model was generated by double knockout in neural progenitor cells and faithfully recapitulates molecular and phenotypic glioblastoma features (Costa et al, 2021). Following intracranial injection of mGB1 control and mGB1 *Sox10* knockdown (*Sox10*-KD) neurospheres, mGB1 *Sox10*-KD tumors developed significantly faster than control tumors, showing features consistent with NSC-like glioblastoma, such as invasive growth at the tumor edges and invasion of the contralateral hemisphere (Fig. EV2A,B) (Wang et al, 2020). RNA-seq data analysis revealed strong enrichment of NSC-like (*P*.adj<0.001) and OLC-like (*P*.adj<0.001) signatures and corresponding marker genes (Wang et al, 2020) in *Sox10*-KD and control tumors, respectively (Fig. 1C,D). The upregulation of the NSC-like glioblastoma marker Sox9 in *Sox10*-KD tumors was confirmed at the protein level by immunohistochemical analysis (Fig. 1E). These data strongly indicate *Sox10* repression as a driver of glioblastoma OLC-like to NSC-like cell-state transition.

To further evaluate this hypothesis, we cultured KD and control cells in serum-free stem cell (SC) and serum-containing differentiating (Diff; 10% FBS) media. Intriguingly, cells appeared unaffected by serum-derived differentiation cues, continuing to grow as free-floating neurospheres, while control cells adopted a more spread-out morphology (Fig. 1F). Western blotting analysis showed that *Sox10*-KD cells upregulated Sox9 and sustained Sox2 expression levels (Fig. 1G). Furthermore, cell-lineage marker analysis by immunofluorescence microscopy revealed the upregulation of the astrocyte-marker Gfap and the essentially unchanged expression of the neuronal marker beta3-tubulin in KD vs. control cells by the supplementation of as little as 2% FBS (Fig. 1H). This observation is consistent with the more NSC/AC-like cell state observed of *Sox10*-low patient tumors (Fig. 1A).

Loss of *SOX10* induces developmental glioblastoma phenotype

To dissect the molecular basis of *Sox10*-KD-mediated cell-state transition, we next performed single-cell RNA sequencing (scRNA-seq) analysis of mouse mGB1 *Sox10*-KD and control syngraft tumors (Fig. 2A). To this end, we intracranially injected GFP-

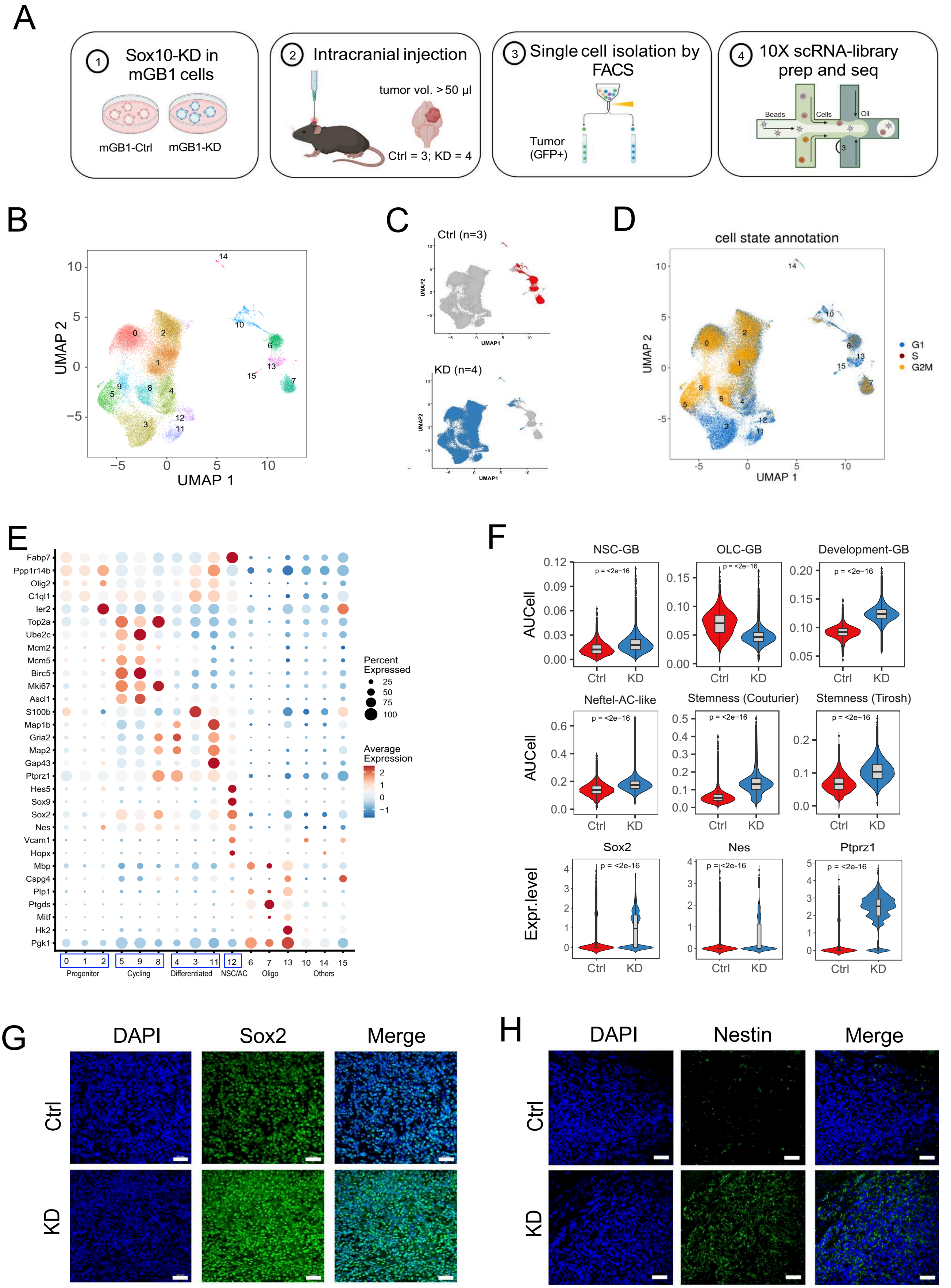
A
1 Sox10-KD in mGB1 cells
mGB1-Ctrl
mGB1-KD
2 Intracranial injection
tumor vol. > 50 µl
Ctrl = 3; KD = 4
3 Single cell isolation by FACS
Tumor (GFP+)
4 10X scRNA-library prep and seq
Beads
Cells
Oil
B
UMAP 2
UMAP 1
0 1 2 3 4 5 6 7 8 9 10 11 12 13 14 15
C
Ctrl (n=3)
KD (n=4)
UMAP1
UMAP2
D
cell state annotation
G1
S
G2M
E
Fabp7
Ppp1r14b
Olig2
C1ql1
Ier2
Top2a
Ube2c
Mcm2
Mcm5
Birc5
Mki67
Ascl1
S100b
Map1b
Gria2
Map2
Gap43
Ptprz1
Hes5
Sox9
Sox2
Nes
Vcam1
Hopx
Mbp
Cspg4
Plp1
Ptgds
Mitf
Hk2
Pgk1
Percent Expressed
25
50
75
100
Average Expression
2
1
0
−1
0 1 2 5 9 8 4 3 11 12 6 7 13 10 14 15
Progenitor
Cycling
Differentiated
NSC/AC
Oligo
Others
F
NSC-GB
OLC-GB
Development-GB
Neftel-AC-like
Stemness (Couturier)
Stemness (Tirosh)
Sox2
Nes
Ptprz1
AUCell
Expr.level
p = <2e−16
Ctrl
KD
G
DAPI
Sox2
Merge
Ctrl
KD
H
DAPI
Nestin
Merge
Ctrl
KD

◀ **Figure 2. scRNA-seq analysis reveals divergent cell fates in control and *Sox10*-KD tumors.**

(**A**) Sample preparation and single-cell sequencing workflow. (**B**) UMAP visualization of tumor cell transcriptional clusters. (**C**) UMAP visualization of tumor cell genotypes (top, control; bottom, *Sox10*-KD); red, control cells; blue, *Sox10*-KD cells. (**D**) UMAP visualization of tumor cell cell cycle phases (G1, blue; S, red; G2/M, yellow). (**E**) Dot plot summarizing the gene expression of the marker genes (*Y* axis) of each transcriptional cluster (*X* axis) shown in (**B**). The main clusters in Sox10-KD tumors are indicated by the boxes at the bottom. (**F**) Violin plots of AUCell scores for selected glioblastoma gene signatures in control and *Sox10*-KD tumor cells: Developmental-like, NSC and OLC-associated, stem cell. Violin plots showing the expression of representative NSC-related genes (*Sox2*, *Nes*, and *Ptprz1*). *P* values were calculated by unpaired two-tailed Wilcoxon's rank-sum tests. $n = 8336$ and 57534 cells in control and KD tumors, respectively. The box-and-whisker plot shows the interquartile range (box), the median AUCell scores or normalized expression values (line inside the box), and the range of data within 1.5 times the interquartile range from the first and third quartiles (whiskers). *P* values were calculated using unpaired two-tailed Wilcoxon's rank-sum tests. (**G**, **H**) Validation of the upregulation of Sox2 (**G**) and Nestin (**H**) in KD tumors. Scale bars = 50 µm. Source data are available online for this figure.

labeled mGB1 control and *Sox10*-KD cells ($n = 8$, each) into C57BL6/J mice. Upon reaching a tumor volume of 50 µl in T2-MRI imaging, 3 control, and 4 KD tumors were harvested, and tumor cells were sorted based on their GFP expression (Fig. EV2C). A total of 65,870 GFP-positive cells were retained after quality control procedures. We further analyzed the copy number variation profiles of GFP-positive cells and identified large-scale chromosomal aberrations previously described in mGB1 (Costa et al, 2021), confirming that the harvested GFP-positive cells are tumor cells (Fig. EV2D).

Unsupervised hierarchical clustering of GFP-positive cells from control and KD tumors identified 16 transcriptional clusters (Fig. 2B; Dataset EV1). Control and KD cells showed distinct transcription patterns and segregated into two cluster groups (Fig. 2C). Cell cycle scoring analysis indicated a higher proportion of cells in the G2/M cell cycle phase in KD than in Ctrl tumors (44.7% in KD vs. 19.3% in Ctrl). Frequent DNA double-strand breaks were not detected in *Sox10*-KD tumors by γH2AX staining, leading us to conclude that the accumulation of cells in G2/M likely was due to the increased growth rate of KD vs. control tumors rather than DNA-damage-induced cell cycle block (Figs. 2D and EV2E–G).

Differential gene expression analysis identified four major groups of clusters within the KD tumors with characteristics of stages of neural development (Fig. 2E). These included clusters expressing markers of stem/progenitor cells (Arai et al, 2005; Wang et al, 2021; Weng et al, 2019) (clusters 0, 1, and 2), intermediate progenitor, and transit-amplifying cells (5, 8, 9), more differentiated progenies along NSC lineage progression (Raponi et al, 2007) (3, 4, 11). Finally, cluster 12 lacked cell cycle markers but showed high expression of *Sox2* and *Nes* and early astrocytes or quiescent NSCs (qNSC) markers such as *Sox9* and the Notch target *Hes5* (Kalamakis et al, 2019; Llorens-Bobadilla et al, 2015).

Gene signature scoring using AUCell (Aibar et al, 2017) revealed an overall association of KD tumors with NSC development. Specifically, KD tumor cells showed significant ($P < 0.001$) enrichment of NSC-associated-glioblastoma and derichment of OLC-associated-glioblastoma signatures (Weng et al, 2019), and enrichment of AC-like GB (Neftel et al, 2019), developmental glioblastoma (Richards et al, 2021), and cancer stemness gene signatures (Couturier et al, 2020; Tirosh et al, 2016). In addition, they strongly upregulated the NSC markers *Sox2*, *Nes*, and *Ptprz1* (Bhaduri et al, 2020), indicative of a more stem/progenitor-like state associated with tumor aggressiveness (Fig. 2F). The stem- and progenitor-like properties of KD tumors also are evident from the increased Sox2 and Nestin protein expression in KD relative to control tumors (Fig. 2G,H).

Sox2 and Nestin are most prominently expressed in the NSC/AC-like potential qNSC cluster 12 (Fig. 2E). GSEA analysis showed enrichment of two qNSC signatures (Kalamakis et al, 2019), qNSC1 (NES = 2.54; *P*.adj<0.001) and qNSC2 (NES = 2,46; *P*.adj<0.001), further indicating the slow-cycling progenitor characteristics of this cell population (Fig. EV2H). Consistent with these results, cell cycle-scoring analysis assigned G0 status not only to the differentiated-cell clusters 3 and 11, but also to the qNSC cluster 12. In contrast, the "progenitor" clusters 0,1, and 2 showed moderately enriched G2/M signatures (Fig. EV2I). Furthermore, double-staining for the stem and progenitor cell marker Sox2 and the proliferation marker Ki67 in KD tumor sections, Sox2-positive/Ki67-negative cells dispersed throughout the tissue, supporting the presence of a slow-cycling potential qNSC population (Fig. EV2J).

In summary, scRNA-seq analysis indicated the *Sox10*-KD-dependent transition to a more neural development-like tumor phenotype, including fast-cycling proliferative and slow-cycling qNSC cell states that potentially contribute to short-term tumor growth and long-term tumor maintenance. These data suggest that effective therapy needs to target both these cell states.

SOX10 suppression enriches a qNSC-like cell state in vitro

We next postulated that *Sox10*-KD leads to comparable cell-state transitions in glioblastoma cell lines, allowing us to use *Sox10*-KD cells as in vitro models to evaluate therapeutic strategies for targeting the quiescent/slow-cycling state. Consistent with this hypothesis, GSEA analysis of mGB1 *Sox10*-KD vs. control RNA-seq data (Wu et al, 2020) showed qNSC (NES = 1.64, adjusted *P* value = 0.0016) and cluster 12 (NES = 1.41, adjusted *P* value = 0.0014) signatures enriched in KD cells (Fig. 3A,B). In addition, qPCR analysis confirmed the upregulation of qNSC-related regulators and markers, including *Sox9* (Llorens-Bobadilla et al, 2015) and *Lrig1* (Marques-Torrejon et al, 2021) (Fig. 3C). Furthermore, *Sox10*-KD increased the abundance of SOX9-positive cells and cells double-positive for SOX9 and the quiescent-cell marker (Coats et al, 1996; Oki et al, 2014) and cell cycle regulator p27 (Fig. 3D,E). We additionally analyzed *Sox10*-KD cells using DNA/Ki67 staining, confirming that KD cells reversibly exited the cell cycle and remained at the G0 phase in reduced growth factor conditions (Fig. EV3A). In line with these findings, we observed p27, *SOX9*, and *LRIG1* upregulation in human NCH441 and NCH644 *SOX10*-KD stem-like tumor cells (Fig. EV3B–D). Immunofluorescence analysis further revealed increased SOX9 and p27 double-positive cells upon *SOX10* downregulation, accompanied by enhanced tumorigenicity in

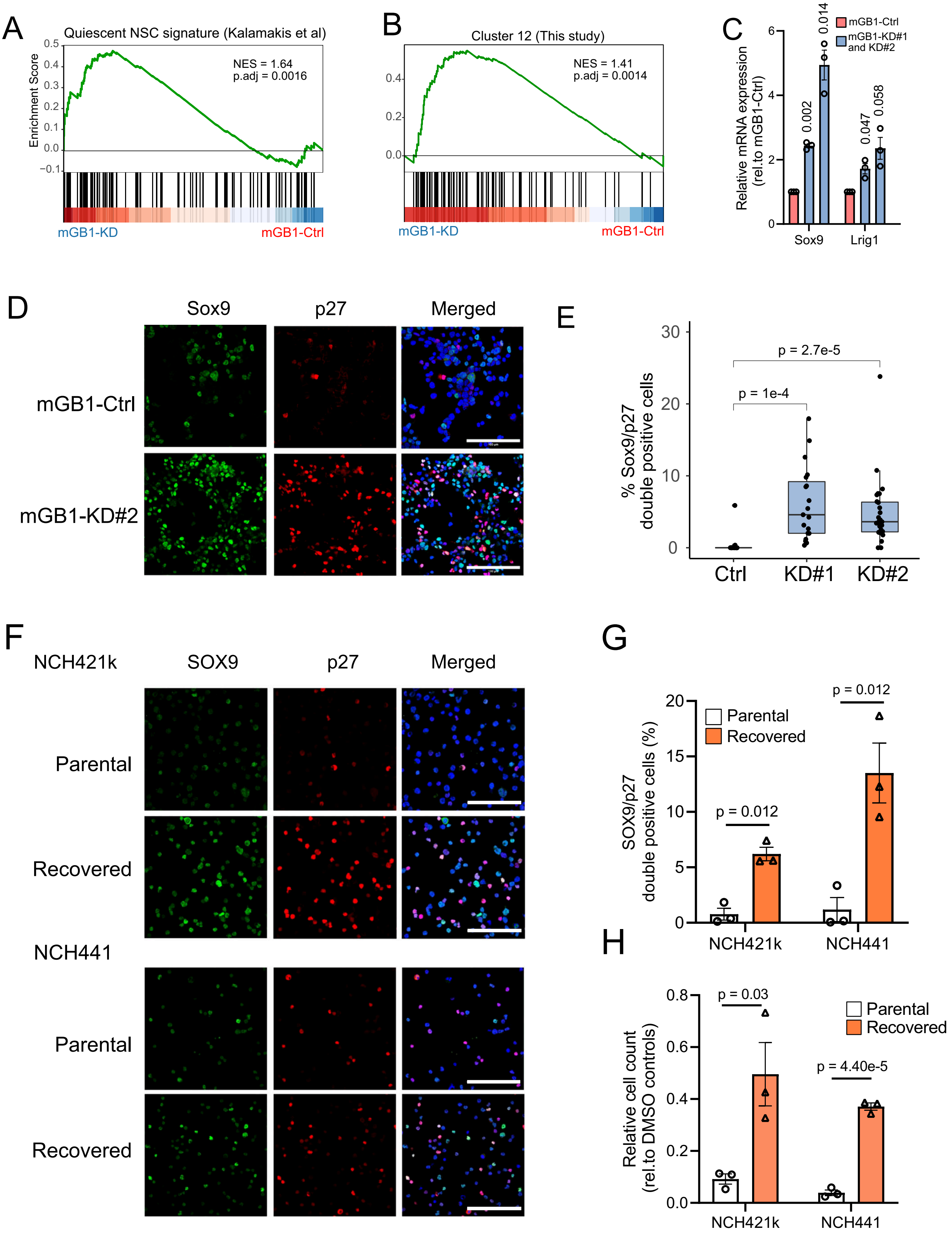
A
Quiescent NSC signature (Kalamakis et al)
Enrichment Score
0.5
0.4
0.3
0.2
0.1
0.0
−0.1
NES = 1.64
p.adj = 0.0016
mGB1-KD
mGB1-Ctrl
B
Cluster 12 (This study)
0.4
0.2
0.0
NES = 1.41
p.adj = 0.0014
mGB1-KD
mGB1-Ctrl
C
Relative mRNA expression (rel.to mGB1-Ctrl)
0
2
4
6
0.002
0.014
0.047
0.058
mGB1-Ctrl
mGB1-KD#1 and KD#2
Sox9
Lrig1
D
Sox9
p27
Merged
mGB1-Ctrl
mGB1-KD#2
E
% Sox9/p27 double positive cells
0
10
20
30
p = 2.7e-5
p = 1e-4
Ctrl
KD#1
KD#2
F
NCH421k
SOX9
p27
Merged
Parental
Recovered
NCH441
Parental
Recovered
G
SOX9/p27 double positive cells (%)
0
5
10
15
20
Parental
Recovered
p = 0.012
p = 0.012
NCH421k
NCH441
H
Relative cell count (rel.to DMSO controls)
0.0
0.2
0.4
0.6
0.8
p = 0.03
p = 4.40e-5
Parental
Recovered
NCH421k
NCH441

Figure 3. ***SOX10*** **suppression promotes quiescent stem cell-like characteristics.**

(**A**) GSEA plot showing the enrichment of a qNSC gene signature in mGB1 *Sox10*-KD over control cells. NES, normalized enrichment score; *P*.adj, adjusted *P* values calculated using the Benjamini–Hochberg method. (**B**) GSEA plot showing the enrichment of Cluster-12 (Fig. 2E) qNSC signature in mGB1 *Sox10*-KD over control cells. The Cluster-12 gene signature comprises the significantly upregulated genes in Cluster 12 with a log2 fold greater than 0.5. Genes were pre-ranked by their log2 expression values in *Sox10*-KD over control cells. NES normalized enrichment scores, *P*.adj adjusted *P* values calculated using the Benjamini–Hochberg method. (**C**) Quantification of the relative expression of the qNSC markers *Sox9* and *Lrig1* by quantitative real-time PCR. Mean values ± SEM relative to mGB1 control from three independent experiments. *P* values were calculated using one-sample *T* tests. (**D**) Immunofluorescence co-staining of Sox9 (green) and p27 (red) in mGB1 control and *Sox10*-KD cells under reduced growth factor conditions (1 ng/ml FGF and 1 ng/ml EGF). Blue: DAPI; scale bar: 100 µm. (**E**) Quantification of Sox9 and p27 double-positive cells. $n = 19$–27 images; The box-and-whisker plot shows the interquartile range (box), the median values (line inside the box), and the range of data within 1.5 times the interquartile range from the first and third quartiles (whiskers). *P* values computed by two-tailed unpaired *T* tests. (**F**) Immunofluorescence co-staining of SOX9 (green) and p27 (red) in NCH421k and NCH441 parental cells and cells that have recovered from (continued) 100 µM temozolomide treatment. Blue: DAPI; Scale bar = 100 µm. (**G**) Quantification of *SOX9*/p27 double-positive cells. Mean ± SEM from three experiments. *P* values were calculated using two-tailed Students' *T* tests. (**H**) Cell numbers of NCH421k and NCH441 parental and recovered cells. Cell counts were normalized to their respective DMSO controls. Mean ± SEM from three experiments. *P* values were calculated using two-tailed unpaired *t* tests. Source data are available online for this figure.

cerebral organoids (Fig. EV3E). In addition, analysis of a curated brain tumor stem cell transcriptome dataset (Marques et al, 2021) ($n = 144$, 116 independent lines) indicated that *SOX10*-low brain tumor stem cells are enriched for qNSC (Kalamakis et al, 2019) and quiescent stem cell tumor cell (Xie et al, 2022) signature (Fig. EV3F), validating the association of *SOX10*-low and NSC-like state.

Next, we investigated the role of TMZ chemotherapy in the emergence of the p27/SOX9 double-positive state in human glioblastoma cells. To this end, we treated human glioblastoma spheroid cultures with TMZ for 4–5 weeks, after which TMZ was withdrawn and allowed to recover. We observed that the fully recovered cells grew slower than the respective parental cells (Fig. EV3G), were enriched for SOX9/p27 double-positive cells (Fig. 3F,G), and were less sensitive to TMZ than the parental cells (Fig. 3H), suggesting that qNSC-like tumor cells induced by TMZ treatment were maintained in the recovered cells. Immunofluorescence analysis of mouse glioblastoma (Rusu et al, 2019) also confirmed the enrichment of Sox9 and p27-positive cells in TMZ-treated animals (Fig. EV3H).

Collectively, our in vitro analysis indicates that *SOX10* suppression by genetic knockdown or TMZ treatment transitioned human and mouse glioblastoma to a qNSC-like cell state, supporting the use of *SOX10*-KD as an in vitro model for therapy-associated phenotypic transition in glioblastoma.

Depletion of qNSCs prolongs survival and induces phenotypic plasticity

We next used the *Sox10*-KD cell model to investigate the targeting of the slow-cycling qNSC-like tumor cells. However, since direct-targeting of these cells is typically hampered by their high therapy resistance, we applied a "lock-out" therapeutic strategy that transitions the quiescent state to a faster-cycling state that is more amenable to antiproliferative pharmacologic inhibition (Saito et al, 2010; Takeishi et al, 2013).

Notch pathway activity is crucial in maintaining the slow-cycling stem cell state, particularly in NSC development (Guentchev and McKay, 2006; Imayoshi et al, 2010). Application of the gamma-secretase inhibitor LY411575 at a sublethal concentration of 2 µM resulted in the marked reduction of the NICD and an increase of the cell cycle regulator cyclin D1 at the protein level in mBG1 cells (Fig. 4A). This was accompanied by a drastic decrease in the expression of the Notch target Hes5 and upregulation of the activated NSC-marker Ascl1 (Fig. 4B), indicating that LY411575 efficiently suppresses Notch pathway activity in *Sox10*-KD cells. Upregulation of Notch target genes was also observed upon *SOX10*-KD in both mouse and human patient-derived tumor spheres (Fig. EV4A). Furthermore, LY411575 significantly reduced the fraction of p27-positive cells in *Sox10*-KD (Fig. 4C,D) but not control cultures (Fig. EV4B,C). In line with this hypothesis, the proportion of 5-Ethynyl-2′-deoxyuridine (Edu)-positive cells was increased by LY411575 treatment (Fig. 4E). These data suggest that Notch inhibition can transition *Sox10*-KD slow-cycling qNSCs toward a faster-cycling cell state.

To test whether LY411575 sensitizes *Sox10*-KD cells to antiproliferative treatment, we performed combination treatments of LY411575 with 78 compounds targeting various proliferation-related signaling pathways, including the ERK and PI3K-mTOR pathways, redox homeostasis and epigenetic regulation (Reagents and Tools Table). Applying a sensitivity index (Chen et al, 2020) threshold of 0.2, we identified several inhibitors with potential LY411575-synergistic effects in KD cells (Fig. 4F). We chose Fimepinostat for further validation, given its favorable safety profile (Younes et al, 2016), wide-ranging inhibitory effect and anti-tumor activity in a preclinical pediatric brain tumor model (Pal et al, 2018; Qian et al, 2012). Pre-treatment of mGB1 *Sox10*-KD cells with LY411575 enhanced their killing by Fimepinostat in the low-nanomolar range (Fig. 4G) and significantly ($P = 0.031$) increased the percentage of apoptotic KD cells (Fig. 4H). Furthermore, analogous to the *Sox10*-KD conditions, a distinct, though statistically not significant, sensitization to Fimepinostat antiproliferative treatment was observed in TMZ-treated human glioblastoma control cells (Fig. EV4D).

Finally, we tested the efficacy of our combination therapy in vivo using our Sox10-KD glioblastoma syngeneic mouse model. Upon most tumors reaching tumor sizes of 2×10^5 radiation units by bioluminescence imaging (about 50 days post injection), we randomized the mice into either vehicle or a combination of Fimepinostat and LY411575 (Combo) groups (Fig. 5A). Tumor growth was inhibited by the combination treatment (Fig. 5B), resulting in a significant extension of overall survival ($P = 0.018$; log-rank test) compared to the vehicle control (Fig. 5C). Consistent with this finding, histological analyses revealed a significant reduction of proliferating cells in tumors of the

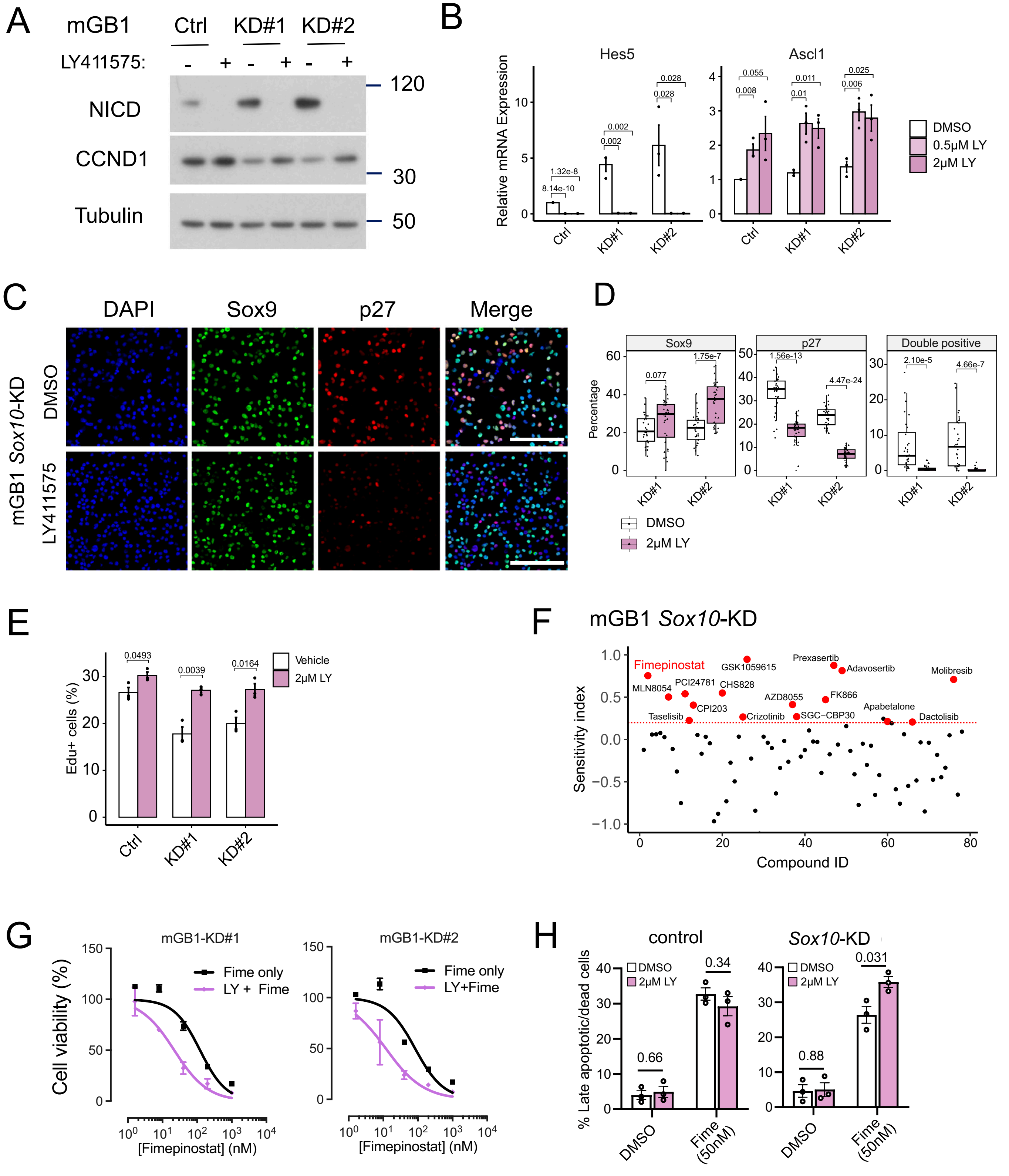

treatment groups (Fig. 5D,E). Fimepinostat alone similarly reduced tumor cell proliferation and extended animal survival, but to a lesser extent than the combination treatment (Fig. EV5).

To characterize cell-state changes associated with treatment responses, we performed scRNA-seq from samples harvested on day 10 after the initiation of treatment. After removing immune and stromal cells from the dataset, we identified 25,494 tumor cells in 4 samples ($n = 2$ in each group) arranged in 15 transcriptional clusters (Fig. 6A). Following our previous analysis, tumors from the vehicle group showed an overall resemblance to developmental-like

Figure 4. Notch inhibition sensitizes KD cells to Fimepinostat treatment.

(**A**) Western blot analysis of Notch intracellular domain (NICD) fragment and cyclin D1 in mGB1 control and *Sox10*-KD cells treated with 2 μM LY411575 for 48 h. Tubulin was used as a loading control. (**B**) mRNA expression of the Notch target gene Hes5 upon DMSO or LY411575 treatment at 0.5 μM and 2 μM for 48 h. Shown are mean expression values ± SEM. *n* = 3 biological replicates. *P* values were calculated with two-tailed unpaired *t* tests. (**C**) Immunofluorescence images of mGB1-KD cells stained with Sox9 and p27 and cultures in reduced growth factor conditions with and without LY411575 treatment. Scale bars = 100 μm. (**D**) Percentages of Sox9-positive, p27-positive and Sox9 and p27 double-positive cells. The box-and-whisker plot shows the interquartile range (box), the median values (line inside the box), and the range of data within 1.5 times the interquartile range from the first and third quartiles (whiskers). *n* = 32–33 images per condition. *P* values were computed using two-tailed unpaired *T* tests. (**E**) Bar plots show the percentages of Edu-incorporated cells under each condition. Mean ± SEM from three experiments. *P* values were calculated using a two-tailed unpaired *t* test. (**F**) Summary of the results of the compound screen in mGB1 *Sox10*-KD (KD#2) cells. The effectiveness of the combination with LY411575 pre-treatment was evaluated by sensitivity index. Compounds that were sensitized by LY411575 treatment (defined as a sensitivity index above 0.2) were labeled red. (**G**) Dose-response curves of Fimepinostat alone (black curve) and LY411575 + Fimepinostat (purple curve) in mGB1 *Sox10*-KD cells (KD#1 and KD#2). Shown are the mean ± SD of the cell viability (%) from three biological replicates. (**H**) Bar plots showing the percentages of late-apoptotic cells (Annexin-V and Live/Dead staining double-positive cells) in mGB1 control and *Sox10*-KD cells. Shown are the median values ± SEM. *P* values were computed using two-tailed unpaired *T* tests. Source data are available online for this figure.

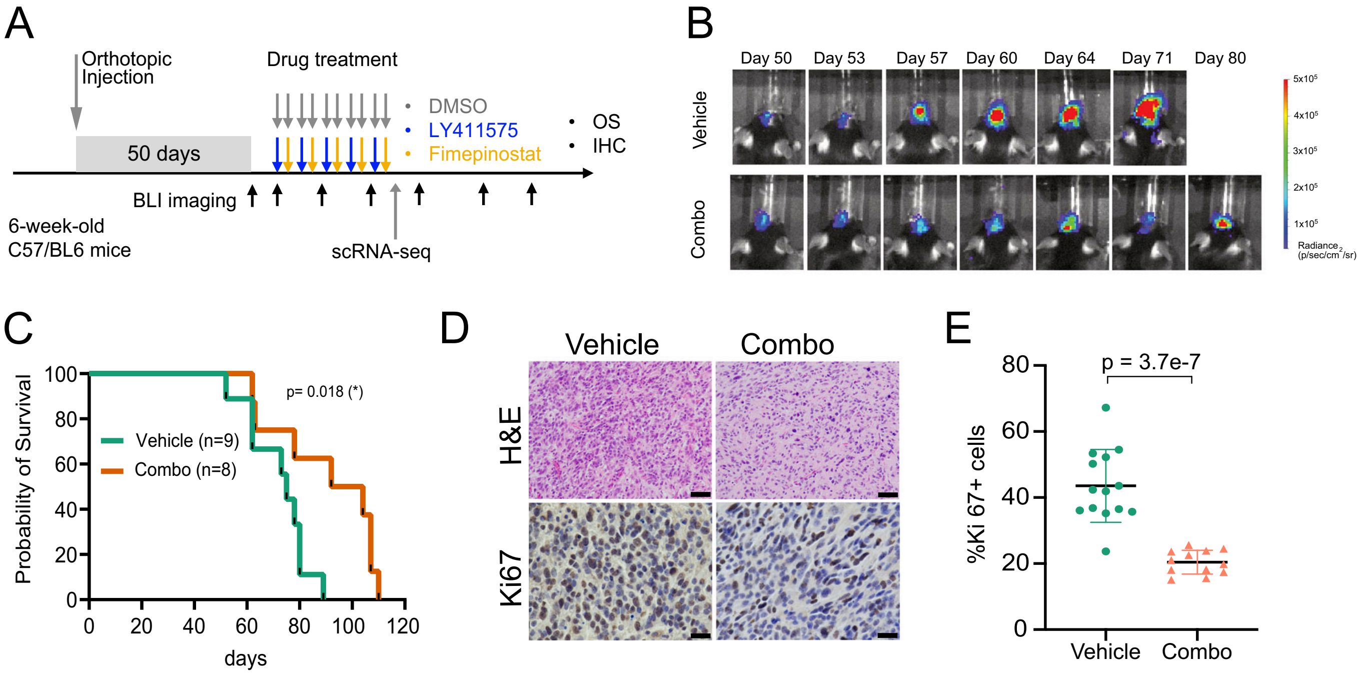

Figure 5. In vivo validation of combination treatment.

(**A**) Schematic summarizing in vivo drug testing experiments. mGB1 *Sox10*-KD cells (KD#2) were orthotopically injected. Upon engraftment and tumor growth, as evidenced by the bioluminescence imaging, animals were randomized into either Vehicle (*n* = 9) or combination (Combo) treatment groups (*n* = 8). In the combination treatment group, the drugs (100 mg/kg Fimepinostat + 10 mg/kg LY411575, p.o.) were delivered on alternating days for five cycles (total of 10 days). (**B**) Tumor growth visualized by bioluminescence imaging in the Vehicle and Combo groups. (**C**) Kaplan–Meier survival curves of mice intracranially injected with KD cells in Vehicle (*n* = 9) and Combo groups (*n* = 8), respectively. Log-rank test was used to calculate the *P* value indicated in the plot. (**D**) H&E and Ki67 staining of end-stage tumors of each treatment group. Scale bars = 50 μm (H&E) and 20 μm (Ki67 IHC). (**E**) Quantification of Ki67 positive cells in (**D**). Shown are the median values ± interquartile ranges. *P* values were calculated with two-tailed unpaired *T* tests (*n* = 12–14 images from three different animals in each group). Source data are available online for this figure.

glioblastoma, including qNSC (cluster 11) and proliferative cell populations. UMAP analysis of the individual tumors from the treatment and control groups revealed that the combination treatment depleted the Notch-high clusters 5, 8, and 11 and the proliferative clusters 4 and 5, indicating the specificity of the treatment (Fig. 6B,C). Notably, the combination treatment strategy also resulted in the emergence of new clusters 9, 10, and 13, which were enriched for qNSC and mesenchymal features (Fig. 6D).

Additional analysis of all tumor cells indicated that the combination therapy diverted the tumors from cellular states reminiscent of normal neural development (developmental glioblastoma) toward inflammatory wound response-related states (injury glioblastoma), along a recently proposed transcriptional gradient (Richards et al, 2021) (Fig. 6E). This observation was further supported by signature scoring of the corresponding developmental and injury genesets (Fig. 6F).

Discussion

In recent years, numerous scRNA-Seq studies have emphasized the remarkable phenotypic plasticity of glioblastoma cells (Yabo et al,

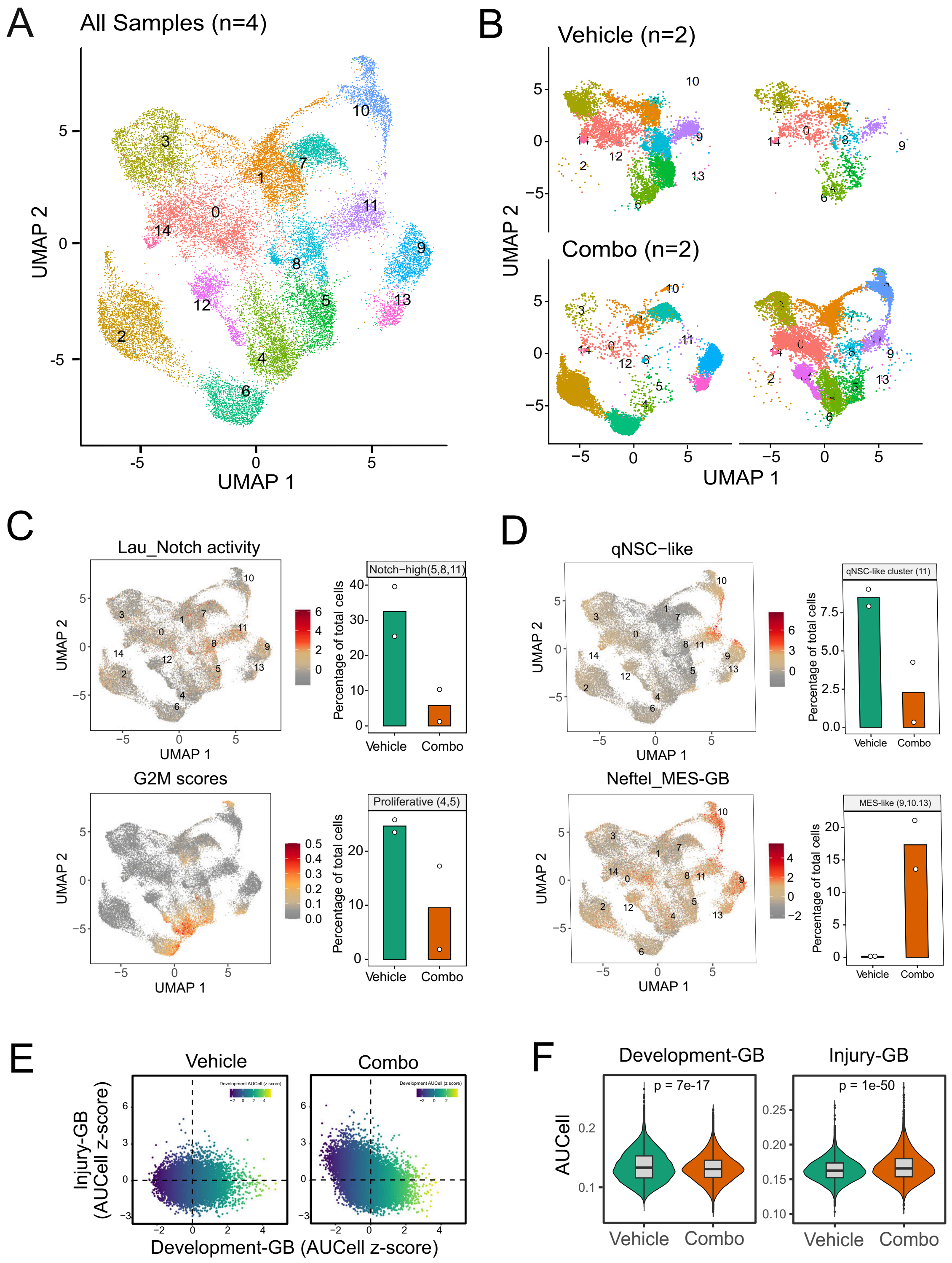

2022) and revealed a phenotypic space defined by neurodevelopmental state and stress adaptation (Garofano et al, 2021; Neftel et al, 2019; Richards et al, 2021). However, the mechanisms and translational consequences of phenotypic plasticity remain largely unexplored. Here, we showed that *SOX10* governs glioblastoma plasticity by mediating the transition between two clinically relevant cell states. Single-cell analyses further revealed the emergence of the quiescent stem cell state upon *Sox10* downregulation, reminiscent of the cell-state transition mediated by TMZ treatment. Importantly, we demonstrated the feasibility and effectiveness of designing a treatment strategy guided by the deep characterization of the tumor cell-state landscape.

A recent study demonstrated that the inactivation of tumor suppressors (Tp53, Nf1, and Pten) in mouse oligodendrocyte-lineage cells (OLCs) versus NSC (NSCs) generated glioblastoma with distinct

◀ **Figure 6. scRNA-seq analysis of post-treatment tumors.**

(**A**) UMAP visualization of RNA expression clusters from single-cell sequencing analysis of tumors from two animals per treatment group (total $n = 4$). Tumors were harvested on day 5 after treatment started. (**B**) UMAP visualization of RNA expression clusters of the four individual tumors ($n = 2$ in each group). (**C**) UMAP plots showing the distribution of cells with high Notch (top) and G2M scores (bottom). Bar plots on the right quantify the depletion of clusters with the highest Notch activity (clusters 5, 8, 11) and proliferative scores (clusters 4 and 5) by combination relative to control treatment. The *Y* axis shows the proportion of cells in the indicated clusters relative to all cells sequenced for the respective tumor. Shown are the mean values ± interquartile ranges of the percentage of total cells in two animals in each group. (**D**) UMAP plots showing the distribution of cells with high qNSC-like (top) and MES-GB like scores (bottom). Bar plots on the right quantify the percentages of the cluster with high qNSC-like cell scores (cluster 11) and MES-GB scores (clusters 9, 10, and 13) by combination relative to control treatment. The *Y* axis shows the proportion of cells in the indicated clusters relative to all cells sequenced for the respective tumor. Shown are the mean values ± interquartile ranges of the percentage of total cells in two animals in each group. (**E**) Visualization of the dataset using scaled Developmental and Injury Response AUCell scores as *X* and *Y* axes, respectively. (**F**) Violin plot showing the AUCell scores of Development-GB and Injury-GB. $n = 8160$ and 17,334 cells in Vehicle and Combo groups, respectively. The box-and-whisker plot shows the interquartile range (box), the median AUCell scores (line inside the box), and the range of data within 1.5 times the interquartile range from the first and third quartiles (whiskers). *P* values were calculated using unpaired two-tailed Wilcoxon's rank-sum tests.

phenotypes and therapeutic vulnerabilities (Wang et al, 2020). Here, we showed that the suppression of *SOX10* is sufficient to mediate the transition of OLC-like (*SOX10*-high/*SOX9*-low) to NSC-like (*SOX10*-low/*SOX9*-high) tumor phenotypes, in line with the roles of these transcription factors in determining cell-lineage identities during normal development (Glasgow et al, 2014; Scott et al, 2010; Stolt et al, 2002). Our data further indicate that this phenotypic plasticity is based on the co-option of *SOX10* and *SOX9* regulation in normal development (Reiprich et al, 2017). This antagonistic relationship between *SOX10* and *SOX9* also appears to extend to other cancers, i.e., resulting in melanoma progression upon reduced expression of *SOX10* (Shakhova et al, 2015; Tsoi et al, 2018). This suggests *SOX10* could be a key regulator of phenotypic transition across different cancer types.

Our single-cell sequencing analysis further revealed a heterogeneous cellular architecture of the *Sox10*-KD tumors, characterized by the presence of cycling stem and progenitor cells and a cluster of slow-cycling tumor cells, similar to a type of dormant stem cell that regenerates neural and glial cells after brain injury and in cancer, where quiescent stem cell-like tumor cell populations were associated with tumor initiation and recurrence (Chen et al, 2012; Kalamakis et al, 2019; Llorens-Bobadilla et al, 2015; Xie et al, 2022). Furthermore, we showed that temozolomide treatment suppressed *SOX10* in glioblastoma model systems, resulting in the enrichment of a slow-cycling SOX9/p27 double-positive cell population, suggesting a role for *SOX10*-dependent cell-state transitions in therapy-associated tumor progression. Our results are corroborated by findings suggesting an association between treatment-induced *SOX10* expression and a slow-cycling phenotype in both glioma and melanoma (Capparelli et al, 2022; Cronin et al, 2013; Lau et al, 2015; Sun et al, 2014).

A key question surrounding tumor plasticity is whether we can force therapy-resistant tumor cells to adopt a therapeutically more manageable cell state. The Notch signaling pathway has been implicated in maintaining the slow-cycling NSCs (Boareto et al, 2017; Chapouton et al, 2010; Guentchev and McKay, 2006), glioblastoma stem cells (Liau et al, 2017) and dormant stem cells in other anatomical locations (Aguanno et al, 2019). Here, we showed that *SOX10*-KD leads to decreased Notch pathway activity, potentially through the activation of a positive feedback loop mediated by *SOX9* and *SOX2* (Wang et al, 2019), consistent with our finding of increased protein levels of these factors in KD tumors. We then applied sublethal Notch inhibitor treatment to drive *Sox10*-KD cells out of their slow-cycling phenotype, rendering them sensitive to antiproliferative therapy such as standard radio-chemotherapy (Yahyanejad et al, 2016). On this basis, we hypothesized that Notch inhibitors could also sensitize to the HDAC/PI3K dual inhibitor and suppressor of DNA repair Fimepinostat (Pal et al, 2018). This therapeutic strategy successfully depleted proliferative and slow-cycling qNSC-like tumor cells and significantly extended overall survival in a syngeneic glioblastoma mouse model. However, the applied treatment also markedly re-modeled the tumor-phenotype landscape, leading to the emergence of qNSC-like cell populations with mesenchymal features, representing potential therapy-resistant states. These therapy-induced clusters might be the reason for the modest improvement of survival in the combination treatment group; however, their detailed characterization offers an opportunity to adapt and improve future treatment approaches targeting slow-cycling populations.

In summary, these results show the potential of using phenotypic plasticity information to aid the design and optimization of cancer therapies.

Methods

Reagents and tools table

Primary antibodies			
Name	**Dilution**	**Source**	**Catalog number**
Anti-Cleaved Notch1 (Val1744) (D3B8) rabbit mAB	1:1000 (WB)	Cell Signaling Technology	4147 (RRID:AB_2153348)
Anti-Cyclin D1, mouse mAB	1:1000 (WB)	BD Biosciences	556470 (RRID: AB_396432)
Anti-GFAP antibody, chicken pAB	1:500 (IF)	Millipore	AB5541 (RRID: AB_177521)
Anti-GFP antibody, chicken pAB	1:500 (IF)	Abcam	ab13970 (RRID: AB_300798)
Anti-Ki67, rabbit pAB	1:200 (FC)	Abcam	ab15580 (RRID:AB_443209)

Primary antibodies

Name	Dilution	Source	Catalog number
Anti-p27Kip1, mouse mAB	1:1000 (WB); 1:300 (IF)	BD Biosciences	554069 (RRID:AB_395225)
Anti-*SOX2*, rabbit pAB	1 :1000 (WB)	Millipore	AB5603 (RRID:AB_2286686)
Anti-Sox9 (D8G8H), rabbit mAB	1:1000 (WB); 1:500 (IF)	Cell Signaling Technology	82630 (RRID:AB_2665492)
Anti-α-Tubulin, mouse mAB	1:10000 (WB)	Sigma Aldrich	T9026 (RRID:AB_477593)
Anti-Tubulin b3 (TUBB3), mouse mAB	1:500 (IF)	Biolegend	801201 (RRID:AB_2313773)

Secondary antibodies

Name	Dilution	Source	Catalog number
Anti-mouse IgG Alexa Fluor 647	1:1000	Invitrogen	A-21245
Anti-mouse IgG Alexa Fluor Plus 488	1:1000	Invitrogen	A-32723
Anti-mouse IgG HRP-linked	1:5000	Cell Signaling Technology	7076S
Anti-rabbit IgG Alexa Fluor 488	1:1000	Invitrogen	A-11034
Anti-rabbit IgG HRP-linked	1:5000	Cell Signaling Technology	7074S
Donkey anti-rabbit IgG (H + L), CF647	1:1000	Sigma	SAB4600177
Goat anti-rabbit IgG (H + L), Alexa Fluor 555	1:1000	Invitrogen	A-21428
Goat anti-chicken IgY (H + L) secondary antibody, Alexa Fluor 488	1:1000	Invitrogen	A-11039

Oligonucleotides and other sequence-based reagents

shRNAs	Sequence	Targeting site
Mouse_Sox10_sh1	CCACGAGGTAATGTCCAACAT	Coding region (TRCN0000018985)
Mouse_Sox10_sh2	TTGCTCCAGCGATACCTTAAT	3′ UTR (TRCN0000244290)
Non-targeting shRNA	CAACAAGATGAAGAGCACCAA	NA
sgRNAs	**Sequence**	
Human_SOX10_sg1	ATTCAGGCTCCGTCCTAACG	
Human_SOX10_sg2	CGAGCTGGACCGCACACCTT	
Human_SOX10_sg3	AGTCTCGGGCTGTCCGGCCA	
Negative control	GCGCCAAACGTGCCCTGACGG	
qPCR primers	**Forward sequence**	**Reverse sequence**
Human-SOX10	CTTTCTTGTGCTGCATACGG	AGCTCAGCAAGACGCTGG
Human-SOX9	AGCGAACGCACATCAAGAC	CTGTAGGCGATCTGTTGGGG
Human-LRIG1	GTGTCATCACCAACCACTTTGGC	GCAATCTGAGGGTTTGGGTGAC
Human-NRARP	CAAGGGCAACACGCAGGAGCT	CCGAACTTGACCAGCAGCTTCA
Human-HES5	TCCTGGAGATGGCTGTCAGCTA	CGTGGAGCGTCAGGAACTGCA
Human-TBP	GAACCACGGCACTGATTTTC	CCCCACCATGTTCTGAATCT
Mouse Sox10	GTGCCAGCAAGAGCAAGCCG	CTGCCTTCCCGTTCTTCCGCC
Mouse-Sox9	CACACGTCAAGCGACCCATGAA	TCTTCTCGCTCTCGTTCAGCAG
Mouse-Lrig1	TTCAGCCAACGCTACCCTCACA	TAAGCCAGGTGATGCGTGGTGT
Mouse-Nrarp	CAGACAGCACTACACCAGTCAG	CCGAAAGCGGCGATGTGTAGC
Mouse-Hes5	CCGTCAGCTACCTGAAACACAG	GGTCAGGAACTGTACCGCCTC
Mouse-Tbp	ACCGTGAATCTTGGCTGTAAAC	GCAGCAAATCGCTTGGGATTA

Public datasets	Source
Brain tumor stem cell bulk RNA-seq	Marques et al, 2021
TCGA-GBM (HG-U133A)	TCGA

Drug-screening compounds

Cat no.	Name	Pathways	Target	Receptor
Drug-screening compounds				
Cat no.	Name	Pathways	Target	Receptor
T1952	MK-2206 dihydrochloride	Cytoskeletal signaling; PI3K/Akt/mTOR signaling	Akt	Akt1; Akt2; Akt3
T3132	SC66	Cytoskeletal signaling; PI3K/Akt/mTOR signaling	Akt inhibitor	Akt
T2492	Perifosine	Cytoskeletal signaling; PI3K/Akt/mTOR signaling	Akt inhibitor	Akt
T4489	AZD26	PI3K/Akt/mTOR signaling; cytoskeletal signaling	Akt inhibitor	Allosteric Akt
T1961	Vistusertib	Cytoskeletal Signaling; PI3K/Akt/mTOR signaling; MAPK	Akt inhibitor; mTOR inhibitor; PI3K inhibitor; S6 Kinase inhibitor	P-Akt (S473); mTOR; PI3Kα; pS6 (S235/236)
T1936	Alectinib	Angiogenesis; tyrosine kinase/adaptors; tyrosine kinase/adaptors	ALK inhibitor; tyrosine kinases inhibitor; VEGFR inhibitor	ALK; ALK (F1174L); ALK (R1275Q); INSR; VEGFR2 (KDR)
T1661	Crizotinib	Angiogenesis; tyrosine kinase/adaptors	ALK; c-Met/HGFR	ALK; c-Met
T16156	MT 63-78	PI3K/Akt/mTOR signaling	AMPK; mTOR	AMPK;mTORC1
T2235	Dactolisib	DNA damage/DNA repair; PI3K/Akt/mTOR signaling	ATM/ATR; mTOR; PI3K	ATR; mTOR (p70 S6K); p110α; p110γ; p110δ
T2509	Tozasertib	Cell cycle/checkpoint; chromatin/epigenetic	Aurora Kinase	Aurora A; Aurora B; Aurora C
T6315	MLN8054	Cell cycle/checkpoint; metabolism; angiogenesis; GPCR/G protein; chromatin/epigenetic; stem cells	Aurora kinase inhibitor; casein kinase inhibitor; PKA inhibitor; Src inhibitor	Aurora A; Aurora B; CK2; PKA; Lck
T6458	CYC116	Cell cycle/checkpoint; angiogenesis; PI3K/Akt/mTOR signaling; chromatin/epigenetic; tyrosine kinase/adaptors; MAPK	Aurora Kinase inhibitor; CDK inhibitor; FLT inhibitor; S6 Kinase inhibitor; VEGFR inhibitor	Aurora A; Aurora B; CDK2/CyclinE; CDK9/CyclinT; FLT3; p70 S6K; VEGFR2
T2358	ENMD2076	Cell cycle/checkpoint; angiogenesis; apoptosis; chromatin/epigenetic; tyrosine kinase/adaptors	Aurora kinase inhibitor; c-RET inhibitor;FLT inhibitor; Src inhibitor; VEGFR inhibitor	Aurora A; RET; FLT3; Src; VEGFR3/FLT4; Src
T2378	RGB-286638 free base	Cell cycle/checkpoint	CDK inhibitor	CDK1/cyclinB1; CDK2/cyclinE; CDK3/cyclinE; CDK4/cyclin D1; CDK9/cyclinT1; p35-CDK5
T2029	Bohemine	Cell cycle/checkpoint	CDK inhibitor	CDK
T2247	KenPaullone	PI3K/Akt/mTOR signaling; cell cycle/checkpoint; stem cells	CDK inhibitor; GSK-3 inhibitor	CDK1/CyclinB; CDK2/CyclinA; CDK2/CyclinE; CDK5/p35; GSK-3β
T1778	AT 7519 hydrochloride salt	PI3K/Akt/mTOR signaling; cell cycle/checkpoint; stem cells	CDK inhibitor; GSK-3 inhibitor	CDK2/CyclinA; CDK4/Cyclin D1; CDK5/p35; CDK9/CyclinT; GSK-3β
T4327	Prexasertib dihydrochloride	Cell cycle/checkpoint; PI3K/Akt/mTOR signaling; MAPK	Chk; S6 Kinase	Chk1;Chk2;RSK
T4301	AD80	Tyrosine kinase/adaptors; MAPK; angiogenesis; PI3K/Akt/mTOR signaling; apoptosis	c-RET; Raf; Src; S6 Kinase	RET, RAF, SRC, S6K;RET V804M;RET V804L
T3458	EED226	Chromatin/epigenetic	DNA methyltransferase inhibitor; Histone methyltransferase inhibitor	EED; PRC2
T2377	XL147 analogue	DNA damage/DNA repair; PI3K/Akt/mTOR signaling	DNA-PK inhibitor; PI3K inhibitor	DNA-PK; PI3Kα; PI3Kβ; PI3Kγ; PI3Kδ
T1826	Voxtalisib Analogue	DNA damage/DNA repair; PI3K/Akt/mTOR signaling	DNA-PK inhibitor; PI3K inhibitor	DNA-PK; PI3Kα; PI3Kβ; PI3Kγ; PI3Kδ
T14073	A-485	Chromatin/epigenetic	Epigenetic Reader Domain; Histone Acetyltransferase	CBP/p300;histone acetyltransferase
T2608	CHIR98014	PI3K/Akt/mTOR signaling; angiogenesis; stem cells; tyrosine kinase/adaptors; MAPK	FGFR inhibitor; GSK-3 inhibitor; S6 Kinase inhibitor; Src inhibitor	bFGFR; GSK-3α; GSK-3β; p70 S6K; c-Src

Drug-screening compounds

Cat no.	Name	Pathways	Target	Receptor
T2310	CHIR99021	PI3K/Akt/mTOR signaling; stem cells	GSK-3	GSK-3α; GSK-3β
T1741	AZD1080	PI3K/Akt/mTOR signaling; stem cells	GSK-3 inhibitor	GSK-3α; GSK-3β
T1755	LY2090314	PI3K/Akt/mTOR signaling; stem cells	GSK-3 inhibitor	GSK-3α; GSK-3β
T3067	Tideglusib	PI3K/Akt/mTOR signaling; stem cells	GSK-3 inhibitor	GSK-3β
T1881	AR-A014418	PI3K/Akt/mTOR signaling; stem cells	GSK-3 inhibitor	GSK-3β; GSK-3β
T1957	AZD2858	PI3K/Akt/mTOR signaling; stem cells	GSK-3 inhibitor	GSK-3
T6187	TDZD8	PI3K/Akt/mTOR signaling; stem cells	GSK-3 inhibitor	GSK-3β
T6059	GSK343	Chromatin/epigenetic	Histone methyltransferase inhibitor	EZH1; EZH2
T3057	UNC1999	Chromatin/epigenetic	Histone methyltransferase inhibitor	EZH1; EZH2
T1788	EPZ6438	Chromatin/epigenetic	Histone methyltransferase inhibitor	EZH2; EZH2
T4583	(R)-PFI-2 hydrochloride	Chromatin/epigenetic	Histone methyltransferase inhibitor	SETD7
T1841	UNC0379	Chromatin/epigenetic	Histone methyltransferase inhibitor	SETD8
T2243	Serdemetan	Apoptosis	Mdm2 inhibitor; p53 activator	HDM2; Mdm2; p53
T6159	LY-2584702 free base	PI3K/Akt/mTOR signaling	mTOR	mTOR (p70 S6K)
T1859	AZD8055	PI3K/Akt/mTOR signaling	mTOR	mTOR
T2706	Palomid 529	PI3K/Akt/mTOR signaling	mTOR inhibitor	mTORC1; mTORC2
T1838	INK 128	PI3K/Akt/mTOR signaling	mTOR inhibitor; PI3K inhibitor	mTOR; mTOR; PI3Kα; PI3Kγ; PI3Kδ
T3153	Serabelisib	PI3K/Akt/mTOR signaling	mTOR inhibitor; PI3K inhibitor	mTOR; p110α; p110β; p110γ; p110δ
T1916	Apitolisib	PI3K/Akt/mTOR signaling	mTOR inhibitor; PI3K inhibitor	mTOR; p110α; p110β; p110γ; p110δ
T2357	GSK1059615	PI3K/Akt/mTOR signaling	mTOR inhibitor; PI3K inhibitor	mTOR; PI3Kα; PI3Kβ; PI3Kγ; PI3Kδ
T1861	Omipalisib	PI3K/Akt/mTOR signaling	mTOR inhibitor; PI3K inhibitor	mTORC1; p110α; p110β; p110γ; p110δ
T2619	CH5132799	PI3K/Akt/mTOR signaling	mTOR inhibitor; PI3K inhibitor	mTOR; PI3Kα; PI3Kβ; PI3Kγ; PI3Kδ
T1970	Gedatolisib	PI3K/Akt/mTOR signaling	mTOR inhibitor; PI3K inhibitor	mTOR; PI3Kα; PI3Kγ
T2265	PI3K-IN-2	Others; PI3K/Akt/mTOR signaling; MAPK	Others inhibitor;S6 Kinase inhibitor;PI3K;mTOR	pPKB; pS6;PI3Kα;PI3Kβ;mTOR;PI3Kγ; PI3Kδ
T1827	Buparlisib	PI3K/Akt/mTOR signaling	PI3K	p110α; p110β; p110γ; p110δ; Vps34
T1994	Pictilisib	PI3K/Akt/mTOR signaling	PI3K	p110α; p110β; p110γ; p110δ
T2672	TG100-115	PI3K/Akt/mTOR signaling	PI3K inhibitor	PI3Kα; PI3Kβ; PI3Kγ; PI3Kδ
T2365	Pilaralisib	PI3K/Akt/mTOR signaling	PI3K inhibitor	PI3Kα; PI3Kβ; PI3Kγ; PI3Kδ
T2073	GSK2636771	PI3K/Akt/mTOR signaling	PI3K inhibitor	PI3Kβ
T6168	ZSTK474	PI3K/Akt/mTOR signaling	PI3K inhibitor	PI3K; PI3Kα; PI3Kβ; PI3Kγ; PI3Kδ
T1988	Duvelisib	PI3K/Akt/mTOR signaling	PI3K inhibitor	PI3Kα; PI3Kβ; PI3Kγ; PI3Kδ
T1999	Taselisib	PI3K/Akt/mTOR signaling; metabolism	PI3K inhibitor; Carbonic Anhydrase	PI3Kα; PI3Kβ; PI3Kγ; PI3Kδ;C2β
T2008	LY294002	PI3K/Akt/mTOR signaling; DNA damage/DNA repair	PI3K; DNA-PK	p110α; p110β; p110δ;DNA-PK
T6250	H 89 2HCl	GPCR/G protein; PI3K/Akt/mTOR signaling; MAPK	PKA; S6 kinase	PKA; S6K1
T3518	GSK269962A	Cell cycle/checkpoint; cytoskeletal signaling; PI3K/Akt/mTOR signaling; stem cells; MAPK	ROCK inhibitor; S6 kinase inhibitor	MSK1; ROCK1; ROCK2; RSK1
TN1712	Gossypin	PI3K/Akt/mTOR signaling; MAPK	S6 kinase	RSK2
T6S1302	Carnosol	PI3K/Akt/mTOR signaling; MAPK	S6 kinase	RSK2
T22422	S6K-18	PI3K/Akt/mTOR signaling; MAPK	S6 kinase	S6K1
T2002	PF4708671	PI3K/Akt/mTOR signaling; MAPK	S6 kinase inhibitor	p70 S6K
T1746	LY-2584702 tosylate	PI3K/Akt/mTOR signaling; MAPK	S6 kinase inhibitor	p70 S6K

Drug-screening compounds

Cat no.	Name	Pathways	Target	Receptor
T6877	LJH685	PI3K/Akt/mTOR signaling; MAPK	S6 kinase inhibitor	RSK1; RSK2; RSK3
T6878	LJI308	PI3K/Akt/mTOR signaling; MAPK	S6 kinase inhibitor	RSK1; RSK2;RSK3
T4488	GSK25	PI3K/Akt/mTOR signaling; PI3K/Akt/mTOR signaling; MAPK	S6 kinase inhibitor; mTOR inhibitor	RSK1; mTOR (p70 S6K)
T5428	BIX 02565	PI3K/Akt/mTOR signaling; autophagy; MAPK	S6 kinase; LRRK2	RSK2;LRRK2
T2510	Galunisertib	Stem cells	TGF-beta/Smad	TβRI
T1293	Gatifloxacin	DNA damage/DNA repair	Topoisomerase inhibitor	Topo IV
T1878	XAV939	Stem cells; cytoskeletal signaling	Wnt/beta-catenin	TNKS1; TNKS2
T2237	ICG001	Cytoskeletal signaling; stem cells; chromatin/epigenetic	Wnt/beta-catenin inhibitor; Epigenetic Reader Domain	Wnt/β-catenin; CBP
T2436	GSK2801	Chromatin/epigenetic	Epigenetic Reader Domain inhibitor	BAZ2A/2B
T6668	SGC-CBP30	Chromatin/epigenetic	CREBBP/EP300 inhibitor	CREBBP/EP300
T2452	C646	Chromatin/epigenetic	Histone acetyltransferase inhibitor	p300/CBP
T6133	Remodelin	Chromatin/epigenetic	Histone acetyltransferase inhibitor	Acetyltransferase NAT10

Cell culture

Patient-derived tumorspheres NCH421k, NCH441 and NCH644 were previously characterized and provided by Christel Herold-Mende (Campos et al, 2010). Cells were maintained in stem-like conditions in DMEM/F12 (Gibco,11330-057) containing 1× B27 (without vitamin A) (Gibco, 12587101), 2 mM L-glutamine, 20 ng/ml Epidermal growth factor (Gibco, PHG0311), 20 ng/ml fibroblast growth factor 2 (PeproTech, 100-18B) and 1% Pen/Strep. Cells were maintained as spheres in suspension culture vessels. Large spheres were dissociated with Accutase at 37 °C with occasional agitation Mouse glioblastoma cell line mGB1 was provided by P Angel and was maintained in similar culture conditions with the addition of 1× N2 (Gibco, 17502048). All cell lines were kept in a 5% CO_2 humidified incubator at 37 °C.

SOX10 knockdown

In mGB1 cells, *Sox10* was stably knocked down using short hairpin RNA (shRNA) as previously described (Wu et al, 2020). Briefly, non-overlapping target sequences of shRNA sequences (sh1: TRCN0000018985; sh2: TRCN0000244290; Reagents and Tools Table) were cloned into pLKO.1-puro (Sigma, SHC002). For the delivery of shRNAs, lentiviruses of pLKO.1-non target control, sh1 and sh2 were produced and transduced into mGB1 cells. Transduced cells were selected with 1 μg/ml puromycin for 48 h and the KD efficiency was checked by both qPCR and western blot.

In human GSCs, *SOX10* was stably knocked down using CRISPR-interference method (CRISPRi) as previously described (Wu et al, 2020). Single clones stably expressing pHR-SFFV-dCas9-BFP-KRAB (Addgene, 46911) were expanded and transduced with single guide RNA (sgRNA; Reagents and Tools Table) plasmids previously described. To knock down *SOX10* expression, NCH441 and NCH644 stable clones stably expressing dCas9 were transduced with sgRNA plasmids. Transduced cells were selected with 1 μg/ml puromycin for 48 h and the KD efficiency was checked by both qPCR and western blot.

RNA extraction and reverse transcription quantitative PCR (RT-qPCR)

Cell pellets were first collected, and total RNA was extracted with the RNAeasy Mini Kit and reverse-transcribed into complementary DNA (cDNA) using Quantitect Reverse Transcription Kit (Qiagen, 205311), following the manufacturer's instructions. For mRNA quantification, SYBR-green-based qPCR was performed using 1× primaQuant SYBR Green reagent (Steinbrenner, SL-9902B). Primers used in qPCR are listed in the Reagents and Tools Table.

Western blot

Cells were washed with ice-cold PBS and were lysed in RIPA lysis buffer supplemented with 1× cOmplete™, Mini EDTA-free Protease Inhibitor Cocktail and 1× phosphatase inhibitor phosSTOP. A total of 5 μg of protein samples were loaded and resolved on 4–12% of NuPAGE™ Bis-Tris Protein gels (Life Technologies, NP0335). The proteins were then transferred onto PVDF membrane. The membranes were blocked in 5% skimmed milk or 5% bovine serum albumin, before incubation with primary antibodies overnight (SOX10, SOX9, SOX2, NICD, tubulin). Corresponding horseradish peroxidase (HRP) conjugated secondary antibodies were then added. ECL substrates (Life Technologies, 32132) were then added and were subsequently detected by light-sensitive films. Alpha-tubulin served as the loading control. Primary and secondary antibodies used for Western blots were summarized in the Reagents and Tools Table.

In vivo study

Animal experiments in this study were performed in accordance with relevant ethical regulations and were approved by the

Regierungspräsidium Karlsruhe, Germany (reference no. G-156-15) and in Shanghai, China. *Sox10* was knocked down in mGB1 cells as described above. Prior to intracranial injection, adult C57B6/J mice (8 weeks female) were ordered from Janvier and were allowed to acclimatize in the animal housing facility. For intracranial injection, 200,000 cells (Ctrl and KD cells, in 1 µl volume) were injected into adult C57B6/J mice (8 weeks female) brain under anesthesia with isoflurane. For drug studies, luciferase-expressing mGB1-KD cells were used and injected as indicated above. Tumor growth for single-cell analysis, tumor growth was monitored by MRI scanning 1 month after injection. For drug studies, tumor growth was monitored by bioluminescence imaging by i.p. injection of D-luciferin. Animals were randomized into treatment groups based on estimated tumor size prior to treatment start. Sample or treatment blinding was not applied. The sample size was determined by simulation using R analysis software. In the combination treatment group, the drugs (100 mg/kg Fimepinostat + 10 mg/kg LY411575, p.o.) were delivered on alternating days for five cycles (total of 10 days).

Single-cell library preparation and sequencing

Mice with large tumor sizes (above 50 µl as measured by T2 MRI) in both groups were sacrificed and included in this study (4 mice from KD, 3 mice from Ctrl). After euthanization with carbon dioxide, tumor areas were carefully resected to ensure minimal inclusion of normal brain tissue. Tumors were then finely minced and dissociated using Tumor Dissociation Kit, mouse using gentleMACS dissociator (Miltenyi Biotech, 130-096-730), according to manufacturers' instructions. The cell pellets were then resuspended in 1% BSA/PBS and were sorted on BD FACSAria™ Fusion based on GFP-positivity to isolate tumor cells. They were then subject to single-cell capture and library preparation in the singe cell Open Lab in DKFZ, Heidelberg. Single-cell libraries were prepared using Chromium Next GEM Single Cell 3′ GEM, Library & Gel Bead Kit v3.1 (10X P.N.: 1000128), closely following the standard protocols recommended by 10X Genomics. Libraries were quantified using the Qubit dsDNA H.S. Assay kit. Equal amounts of the libraries were pooled and sequenced on NovaSeq 6000 with Paired-end (28 + 94 bp) S2 setup at High Throughput Sequencing Unit of the Genomics and Proteomics Core Facility at the German Cancer Research Center (DKFZ, Heidelberg). For the single-cell study in the drug treatment groups, single-cell RNA-Seq libraries were prepared using SeekOne® MM Single-cell 3' library preparation kit (SeekGene, K00104-04), sequenced on Illumina NovaSeq 6000 with PE150 read length.

Single-cell data analysis

Raw reads in FASTQ format were aligned to the mouse reference genome mm10 version 3.0.0 by conducting the count pipeline within the 10x Cell Ranger software. For each sample, a gene-cell matrix of unique molecular identifier (UMI) counts was generated. The UMI matrices were passed to R using the *Read10x()* function from the Seurat package version 3.2.3 (Stuart et al, 2019), and were converted into a Seurat object via the *CreateSeuratObject()* function, allowing for subsequent filtering, normalization and downstream analyses. Cells with feature counts of 200 or less and cells containing 10% or more mitochondrial RNA, defined as features starting with the character string "mt-", were filtered out. Subsequently, the count matrix was normalized using *NormalizeData()* function: Feature counts for each cell were divided by its total counts, multiplied by 10,000.

The quality of the scRNA-seq data of each sample was evaluated by examining the metadata table of the 10× pipeline, as well as analyzing the number of genes and features per cell and the percentage of mitochondrial RNA. The distribution of cells coming from the same group (e.g., *Sox10*-KD tumor cells) was further assessed in the UMAP space to estimate batch effects. To determine the differentially expressed genes (DEGs) of each cluster (Dataset EV1), FindAllMarkers () function from the Seurat package was used. The significance of the DEGs was computed using Wilcoxon tests with an adjusted (Bonferroni correction) *P* value of 0.05. Gene signature activity in single cells was evaluated using AUCell (v.1.4.1).

TMZ treatment in glioblastoma cell lines

NCH421k and NCH441 were seeded at 100,000 cells per well on six-well plates. Cells were treated with DMSO or temozolomide (TMZ, Sigma, T2577) at 25 µM or 50 µM. TMZ was refreshed every 3–4 days before harvesting protein for WB analyses.

For TMZ pre-treatment prior to combination treatment (Fig. EV4), NCH421k and NCH441 were treated with 50 µM TMZ for 7 days. Then, the cells were dissociated with Accutase, washed and seeded at a density of 10,000 cells/well into a 96-well plate either with LY411575 (4 µM) or without. One day after seeding, Fimepinostat was added to the cells at the indicated concentrations. Forty-eight hours after Fimepinostat treatment, the viability was assessed using the CellTiter-Glo Reagent.

For inducing TMZ-recovered cells, NCH421k and NCH441 were seeded at 100,000 cells per well on six-well plates. TMZ was refreshed every 3–4 days, and viable cells were counted using the TC20 automated cell counter (Biorad #1450102) every week. Tumor cells treated with DMSO reached confluence around 10–14 days after seeding and were counted for 2 weeks, whereas cells treated with TMZ were counted for 5 weeks before temozolomide was withdrawn.

TMZ treatment in cerebral organoid models

NCH644 cells were first transduced with pLenti-PGK-V5-GFP-LUC-Neo. A total of 100,000 NCH644-GFP-luc cells were co-cultured with iPSC-induced cerebral organoids (Linkous et al, 2019). Tumor growth was monitored by bioluminescence signals (BLI). Total proton flux was quantified using the Living Image® software. BLIs before DMSO or 100 µM of TMZ was added to the human cerebral organoid glioma were used as baseline and were measured every 3 days. To analyze the expression of SOX10 in tumor cells after TMZ treatment, tumor cells were harvested and stained with viability dye at 1:500 dilution in PBS for 30 min at 4 °C. Cells were then fixed with 4% PFA (methanol free) for 15 min at R.T. in the dark. Cells were washed with FACS buffer and incubated with permeabilization and blocking buffer (5% normal goat serum in 0.5% Triton X-100) for 1 h at room temperature. After washing with FACS buffer, cells were incubated with rabbit anti-human/mouse SOX10 antibody at 1:500 dilution and chicken anti-GFP antibody at 1:500 dilution in permeabilization and blocking buffer for 1 h at room temperature. Cells were then washed with FACS buffer and stained with conjugated secondary antibodies (anti-rabbit AF647, 1:2000 and anti-chicken AF488, 1:2000) for 30 min at room temperature. Finally, cells were washed and resuspended in FACS buffer and proceeded to flow cytometry analysis. SOX10 expression levels were measured as the median fluorescence intensity (AF647) of the viable, GFP-positive cells. Samples stained with only secondary antibodies were used as a negative control.

Public data analysis

Normalized BTSC and TCGA-GBM data were downloaded from their respective sources (Reagents and Tools Table). Top 25% and bottom 25% of the dataset were classified as *SOX10*-high and *SOX10*-low samples, respectively. Differentially expression analyses were performed using limma package (contrast= *SOX10*-low/*SOX10*-high). Differentially regulated genes, defined as *P*.adj <0.05, were sorted by their log2 fold change and gene set enrichment analyses (GSEA) were performed using the ClusterProfiler package (Yu et al, 2012) against curated genesets. For TCGA-GBM data, only IDH-wildtype primary tumor samples with available *SOX10* expression information were included in the analysis, resulting in 324 samples.

Immunofluorescence staining

For immunofluorescence staining in vitro, cells were seeded on a 12-well immunofluorescence chamber or 96-well plates coated with laminin/poly-L-lysine coating buffer (5 µl laminin + 30 µl poly-L-lysine in 2 ml PBS). Upon proper attachment of the cells, cells were fixed in 4% paraformaldehyde in PBS for 15 min at room temperature. Cells were then washed twice with PBS and permeabilized with ice-cold 0.5% Triton X-100 in PBS for 20 min. They were then blocked with 5% normal goat or donkey serum in 0.5% Triton X-100 in PBS for one hour, before incubating with primary antibodies overnight. The next day, fluorochrome-conjugated secondary antibodies and DAPI or Hoechst-33342 were added. Fluorescence images were captured using an SP8 confocal microscope (for Sox9/p27) and Zeiss Cell Observer epifluorescence microscope equipped with a 10×/0.3 PlnN Ph1 DICI objective (for Gfap/Tubb3). Image analysis software ImageJ and QuPath were used to quantify the number of p27-positive and Sox9/p27 double-positive cells in each image.

For immunostaining in mouse tissue sections, slides were deparaffinized and rehydrated with sequential immersion in xylene, a series of descending concentrations of ethanol (100%, 90%, and 70% ethanol) and finally with distilled water. Next, slides were placed in a cuvette and subjected to heat-induced antigen retrieval. Briefly, slides were immersed in sodium citrate buffer (10 mM sodium citrate, 0.05% Tween-20, pH 6.0) and heated to 100 °C for 20 min using a steam cooker. Slides were allowed to cool down to RT before washing with 0.3% Triton X-100/PBS for 20 min. Afterward, the slides were permeabilized and blocked with 5% normal serum in 0.3% Triton X-100/PBS for 1 h. Primary antibodies were diluted at appropriate concentrations using 0.3% Triton X/PBS supplemented with 1% normal serum. Slides were left in a humidified chamber at 4 °C overnight. The next day, the slides were washed with PBS-T (0.1% Tween-20 in PBS) for three times for 30 min. Fluorochrome-conjugated secondary antibodies were diluted at 1:1000 in PBS-T and were incubated in the dark at RT for 1 h. After secondary antibody incubation, slides were washed with PBS three times for 30 min. Upon the last wash, slides were treated with TrueBlack (Biotium #23007) to reduce autofluorescence according to the manufacturer's instructions. After further washing steps with PBS, slides were mounted using ProLong™ Glass Antifade Mountant with NucBlue™ Stain (Invitrogen, P36983). Fluorescence images were captured with an SP8 confocal microscope. Primary and secondary antibodies used for immunofluorescence were summarized in the Reagents and Tools Table.

G0/G1 cell cycle analyses by flow cytometry

To analyze the distribution of G0 and G1, cells were first spun down and singularized by accutase at 37 °C. For each stain, around 0.5 million cells were used. Cells were fixed with 70% ethanol at 4 °C overnight. The next day, cells were first rehydrated with FACS buffer (2% fetal bovine serum in PBS) and then centrifuged at 9000 rpm for 10 min. Cells were washed again with FACS buffer and were then incubated with Ki67 antibody at 1:200 dilution in FACS buffer 1 h at room temperature. After primary antibody incubation, cells were washed twice with FACS buffer and stained with AF647 conjugated secondary antibody, donkey against rabbit at 1:1000 dilution in FACS buffer in the dark for 30 min at room temperature. Cells were then washed twice with FACS buffer and stained with FxCycle™ Violet Ready Flow™ Reagent (Invitrogen, R37166) in the dark for 30 min at room temperature. Samples stained with secondary antibodies only and samples stained with FxCycle™ Violet Ready Flow™ Reagent were used as secondary controls.

Drug screening

Mouse brain tumor stem cell mGB1 cells were dissociated with Accutase (Invitrogen, 00-4555-56) and seeded into 384-well plates at a density of 2000 cells per well using 12 channel pipettes with or without 2 µM LY411575 (Selleckchem, S2714). The next day, compounds were added at 2 µM using the BRAVO automated liquid handling platform (Agilent Technologies, G5563AA) equipped with a 96-pipette head (Agilent Technologies, G5055A). The 384-well plates were incubated at 37 °C, 5% CO_2 for 48 h. An equal volume of CellTiter-Glo Reagent (Promega, G7570) was added to the wells. medium of 384-well. The luminescence signal was measured by multimode plate reader (Enspire, 2300). The list of compounds used in drug screening was provided in the Reagents and Tools Table.

Graphics

A synopsis image was created with BioRender.com.

Data availability

RNA sequencing and data have been deposited at the European Nucleotide Archive (ENA) under the accession number PRJEB77072.

The source data of this paper are collected in the following database record: biostudies:S-SCDT-10_1038-S44319-024-00258-8.

Expanded view data, supplementary information, appendices are available for this paper at https://doi.org/10.1038/s44319-024-00258-8.

Peer review information

A peer review file is available at https://doi.org/10.1038/s44319-024-00258-8

References

Aguanno S, Petrelli C, Di Siena S, De Angelis L, Pellegrini M, Naro F (2019) A three-dimensional culture model of reversibly quiescent myogenic cells. Stem Cells Int 2019:7548160

Aibar S, Gonzalez-Blas CB, Moerman T, Huynh-Thu VA, Imrichova H, Hulselmans G, Rambow F, Marine JC, Geurts P, Aerts J et al (2017) SCENIC: single-cell regulatory network inference and clustering. Nat Methods 14:1083–1086

Al-Mayhani TF, Heywood RM, Vemireddy V, Lathia JD, Piccirillo SGM, Watts C (2019) A non-hierarchical organization of tumorigenic NG2 cells in glioblastoma promoted by EGFR. Neuro Oncol 21:719–729

Arai Y, Funatsu N, Numayama-Tsuruta K, Nomura T, Nakamura S, Osumi N (2005) Role of Fabp7, a downstream gene of Pax6, in the maintenance of neuroepithelial cells during early embryonic development of the rat cortex. J Neurosci 25:9752–9761

Bhaduri A, Di Lullo E, Jung D, Muller S, Crouch EE, Espinosa CS, Ozawa T, Alvarado B, Spatazza J, Cadwell CR et al (2020) Outer radial glia-like cancer stem cells contribute to heterogeneity of glioblastoma. Cell Stem Cell 26:48–63.e46

Boareto M, Iber D, Taylor V (2017) Differential interactions between Notch and ID factors control neurogenesis by modulating Hes factor autoregulation. Development 144:3465–3474

Brooks LJ, Clements MP, Burden JJ, Kocher D, Richards L, Devesa SC, Zakka L, Woodberry M, Ellis M, Jaunmuktane Z et al (2021) The white matter is a pro-differentiative niche for glioblastoma. Nat Commun 12:2184

Campos B, Wan F, Farhadi M, Ernst A, Zeppernick F, Tagscherer KE, Ahmadi R, Lohr J, Dictus C, Gdynia G et al (2010) Differentiation therapy exerts antitumor effects on stem-like glioma cells. Clin Cancer Res 16:2715–2728

Cancer Genome Atlas Research N (2008) Comprehensive genomic characterization defines human glioblastoma genes and core pathways. Nature 455:1061–1068

Capparelli C, Purwin TJ, Glasheen M, Caksa S, Tiago M, Wilski N, Pomante D, Rosenbaum S, Nguyen MQ, Cai W et al (2022) Targeting SOX10-deficient cells to reduce the dormant-invasive phenotype state in melanoma. Nat Commun 13:1381

Chan JM, Zaidi S, Love JR, Zhao JL, Setty M, Wadosky KM, Gopalan A, Choo ZN, Persad S, Choi J et al (2022) Lineage plasticity in prostate cancer depends on JAK/STAT inflammatory signaling. Science 377:1180–1191

Chapouton P, Skupien P, Hesl B, Coolen M, Moore JC, Madelaine R, Kremmer E, Faus-Kessler T, Blader P, Lawson ND et al (2010) Notch activity levels control the balance between quiescence and recruitment of adult neural stem cells. J Neurosci 30:7961–7974

Chen J, Li Y, Yu TS, McKay RM, Burns DK, Kernie SG, Parada LF (2012) A restricted cell population propagates glioblastoma growth after chemotherapy. Nature 488:522–526

Chen Z, Chen C, Zhou T, Duan C, Wang Q, Zhou X, Zhang X, Wu F, Hua Y, Lin F (2020) A high-throughput drug combination screen identifies an anti-glioma synergism between TH588 and PI3K inhibitors. Cancer Cell Int 20:337

Coats S, Flanagan WM, Nourse J, Roberts JM (1996) Requirement of p27Kip1 for restriction point control of the fibroblast cell cycle. Science 272:877–880

Costa B, Fletcher MNC, Boskovic P, Ivanova EL, Eisemann T, Lohr S, Bunse L, Lower M, Burchard S, Korshunov A et al (2021) A set of cell lines derived from a genetic murine glioblastoma model recapitulates molecular and morphological characteristics of human tumors. Cancers 13:230

Couturier CP, Ayyadhury S, Le PU, Nadaf J, Monlong J, Riva G, Allache R, Baig S, Yan X, Bourgey M et al (2020) Single-cell RNA-seq reveals that glioblastoma recapitulates a normal neurodevelopmental hierarchy. Nat Commun 11:3406

Cronin JC, Watkins-Chow DE, Incao A, Hasskamp JH, Schonewolf N, Aoude LG, Hayward NK, Bastian BC, Dummer R, Loftus SK et al (2013) SOX10 ablation arrests cell cycle, induces senescence, and suppresses melanomagenesis. Cancer Res 73:5709–5718

De Silva MI, Stringer BW, Bardy C (2023) Neuronal and tumourigenic boundaries of glioblastoma plasticity. Trends Cancer 9:223–236

Dirkse A, Golebiewska A, Buder T, Nazarov PV, Muller A, Poovathingal S, Brons NHC, Leite S, Sauvageot N, Sarkisjan D et al (2019) Stem cell-associated heterogeneity in glioblastoma results from intrinsic tumor plasticity shaped by the microenvironment. Nat Commun 10:1787

Gangoso E, Southgate B, Bradley L, Rus S, Galvez-Cancino F, McGivern N, Guc E, Kapourani CA, Byron A, Ferguson KM et al (2021) Glioblastomas acquire myeloid-affiliated transcriptional programs via epigenetic immunoediting to elicit immune evasion. Cell 184:2454–2470.e2426

Garofano L, Migliozzi S, Oh YT, D'Angelo F, Najac RD, Ko A, Frangaj B, Caruso FP, Yu K, Yuan J et al (2021) Pathway-based classification of glioblastoma uncovers a mitochondrial subtype with therapeutic vulnerabilities. Nat Cancer 2:141–156

Gimple RC, Yang K, Halbert ME, Agnihotri S, Rich JN (2022) Brain cancer stem cells: resilience through adaptive plasticity and hierarchical heterogeneity. Nat Rev Cancer 22:497–514

Glasgow SM, Zhu W, Stolt CC, Huang TW, Chen F, LoTurco JJ, Neul JL, Wegner M, Mohila C, Deneen B (2014) Mutual antagonism between Sox10 and NFIA regulates diversification of glial lineages and glioma subtypes. Nat Neurosci 17:1322–1329

Guentchev M, McKay RD (2006) Notch controls proliferation and differentiation of stem cells in a dose-dependent manner. Eur J Neurosci 23:2289–2296

Hanahan D (2022) Hallmarks of cancer: new dimensions. Cancer Discov 12:31–46

Imayoshi I, Sakamoto M, Yamaguchi M, Mori K, Kageyama R (2010) Essential roles of Notch signaling in maintenance of neural stem cells in developing and adult brains. J Neurosci 30:3489–3498

Kalamakis G, Brune D, Ravichandran S, Bolz J, Fan W, Ziebell F, Stiehl T, Catala-Martinez F, Kupke J, Zhao S et al (2019) Quiescence modulates stem cell maintenance and regenerative capacity in the aging brain. Cell 176:1407–1419.e1414

Lau J, Ilkhanizadeh S, Wang S, Miroshnikova YA, Salvatierra NA, Wong RA, Schmidt C, Weaver VM, Weiss WA, Persson AI (2015) STAT3 blockade inhibits radiation-induced malignant progression in glioma. Cancer Res 75:4302–4311

Liau BB, Sievers C, Donohue LK, Gillespie SM, Flavahan WA, Miller TE, Venteicher AS, Hebert CH, Carey CD, Rodig SJ et al (2017) Adaptive chromatin remodeling drives glioblastoma stem cell plasticity and drug tolerance. Cell Stem Cell 20:233–246.e237

Linkous A, Balamatsias D, Snuderl M, Edwards L, Miyaguchi K, Milner T, Reich B, Cohen-Gould L, Storaska A, Nakayama Y et al (2019) Modeling patient-derived glioblastoma with cerebral organoids. Cell Rep. 26:3203–3211.e3205

Llorens-Bobadilla E, Zhao S, Baser A, Saiz-Castro G, Zwadlo K, Martin-Villalba A (2015) Single-cell transcriptomics reveals a population of dormant neural stem cells that become activated upon brain injury. Cell Stem Cell 17:329–340

Marques C, Unterkircher T, Kroon P, Oldrini B, Izzo A, Dramaretska Y, Ferrarese R, Kling E, Schnell O, Nelander S et al (2021) NF1 regulates mesenchymal glioblastoma plasticity and aggressiveness through the AP-1 transcription factor FOSL1. eLife 10:e64846

Marques-Torrejon MA, Williams CAC, Southgate B, Alfazema N, Clements MP, Garcia-Diaz C, Blin C, Arranz-Emparan N, Fraser J, Gammoh N et al (2021) LRIG1 is a gatekeeper to exit from quiescence in adult neural stem cells. Nat Commun 12:2594

Mu P, Zhang Z, Benelli M, Karthaus WR, Hoover E, Chen CC, Wongvipat J, Ku SY, Gao D, Cao Z et al (2017) SOX2 promotes lineage plasticity and antiandrogen resistance in TP53- and RB1-deficient prostate cancer. Science 355:84–88

Neftel C, Laffy J, Filbin MG, Hara T, Shore ME, Rahme GJ, Richman AR, Silverbush D, Shaw ML, Hebert CM et al (2019) An integrative model of cellular states, plasticity, and genetics for glioblastoma. Cell 178:835–849.e821

Oki T, Nishimura K, Kitaura J, Togami K, Maehara A, Izawa K, Sakaue-Sawano A, Niida A, Miyano S, Aburatani H et al (2014) A novel cell-cycle-indicator, mVenus-p27K-, identifies quiescent cells and visualizes G0-G1 transition. Sci Rep 4:4012

Pal S, Kozono D, Yang X, Fendler W, Fitts W, Ni J, Alberta JA, Zhao J, Liu KX, Bian J et al (2018) Dual HDAC and PI3K inhibition abrogates NFkappaB- and FOXM1-mediated DNA damage response to radiosensitize pediatric high-grade gliomas. Cancer Res 78:4007–4021

Qian C, Lai CJ, Bao R, Wang DG, Wang J, Xu GX, Atoyan R, Qu H, Yin L, Samson M et al (2012) Cancer network disruption by a single molecule inhibitor targeting both histone deacetylase activity and phosphatidylinositol 3-kinase signaling. Clin Cancer Res 18:4104–4113

Raponi E, Agenes F, Delphin C, Assard N, Baudier J, Legraverend C, Deloulme JC (2007) S100B expression defines a state in which GFAP-expressing cells lose their neural stem cell potential and acquire a more mature developmental stage. Glia 55:165–177

Reiprich S, Cantone M, Weider M, Baroti T, Wittstatt J, Schmitt C, Kuspert M, Vera J, Wegner M (2017) Transcription factor Sox10 regulates oligodendroglial Sox9 levels via microRNAs. Glia 65:1089–1102

Richards LM, Whitley OKN, MacLeod G, Cavalli FMG, Coutinho FJ, Jaramillo JE, Svergun N, Riverin M, Croucher DC, Kushida M et al (2021) Gradient of developmental and injury response transcriptional states defines functional vulnerabilities underpinning glioblastoma heterogeneity. Nat Cancer 2:157–173

Rusu P, Shao C, Neuerburg A, Acikgoz AA, Wu Y, Zou P, Phapale P, Shankar TS, Doring K, Dettling S et al (2019) GPD1 specifically marks dormant glioma stem cells with a distinct metabolic profile. Cell Stem Cell 25:241–257.e248

Saito Y, Uchida N, Tanaka S, Suzuki N, Tomizawa-Murasawa M, Sone A, Najima Y, Takagi S, Aoki Y, Wake A et al (2010) Induction of cell cycle entry eliminates human leukemia stem cells in a mouse model of AML. Nat Biotechnol 28:275–280

Scott CE, Wynn SL, Sesay A, Cruz C, Cheung M, Gomez Gaviro MV, Booth S, Gao B, Cheah KS, Lovell-Badge R et al (2010) SOX9 induces and maintains neural stem cells. Nat Neurosci 13:1181–1189

Shakhova O, Cheng P, Mishra PJ, Zingg D, Schaefer SM, Debbache J, Hausel J, Matter C, Guo T, Davis S et al (2015) Antagonistic cross-regulation between Sox9 and Sox10 controls an anti-tumorigenic program in melanoma. PLoS Genet 11:e1004877

Stolt CC, Rehberg S, Ader M, Lommes P, Riethmacher D, Schachner M, Bartsch U, Wegner M (2002) Terminal differentiation of myelin-forming oligodendrocytes depends on the transcription factor Sox10. Genes Dev 16:165–170

Stuart T, Butler A, Hoffman P, Hafemeister C, Papalexi E, Mauck 3rd WM, Hao Y, Stoeckius M, Smibert P, Satija R (2019) Comprehensive integration of single-cell data. Cell 177:1888–1902.e1821

Stupp R, Mason WP, van den Bent MJ, Weller M, Fisher B, Taphoorn MJ, Belanger K, Brandes AA, Marosi C, Bogdahn U et al (2005) Radiotherapy plus concomitant and adjuvant temozolomide for glioblastoma. New Engl J Med 352:987–996

Sun C, Wang L, Huang S, Heynen GJ, Prahallad A, Robert C, Haanen J, Blank C, Wesseling J, Willems SM et al (2014) Reversible and adaptive resistance to BRAF(V600E) inhibition in melanoma. Nature 508:118–122

Suva ML, Rheinbay E, Gillespie SM, Patel AP, Wakimoto H, Rabkin SD, Riggi N, Chi AS, Cahill DP, Nahed BV et al (2014) Reconstructing and reprogramming the tumor-propagating potential of glioblastoma stem-like cells. Cell 157:580–594

Tabatabai G, Frank B, Mohle R, Weller M, Wick W (2006) Irradiation and hypoxia promote homing of haematopoietic progenitor cells towards gliomas by TGF-beta-dependent HIF-1alpha-mediated induction of CXCL12. Brain 129:2426–2435

Takeishi S, Matsumoto A, Onoyama I, Naka K, Hirao A, Nakayama KI (2013) Ablation of Fbxw7 eliminates leukemia-initiating cells by preventing quiescence. Cancer Cell 23:347–361

Tirosh I, Venteicher AS, Hebert C, Escalante LE, Patel AP, Yizhak K, Fisher JM, Rodman C, Mount C, Filbin MG et al (2016) Single-cell RNA-seq supports a developmental hierarchy in human oligodendroglioma. Nature 539:309–313

Tsoi J, Robert L, Paraiso K, Galvan C, Sheu KM, Lay J, Wong DJL, Atefi M, Shirazi R, Wang X et al (2018) Multi-stage differentiation defines melanoma subtypes with differential vulnerability to drug-induced iron-dependent oxidative stress. Cancer Cell 33:890–904.e895

Verhaak RG, Hoadley KA, Purdom E, Wang V, Qi Y, Wilkerson MD, Miller CR, Ding L, Golub T, Mesirov JP et al (2010) Integrated genomic analysis identifies clinically relevant subtypes of glioblastoma characterized by abnormalities in PDGFRA, IDH1, EGFR, and NF1. Cancer Cell 17:98–110

Wang J, Xu SL, Duan JJ, Yi L, Guo YF, Shi Y, Li L, Yang ZY, Liao XM, Cai J et al (2019) Invasion of white matter tracts by glioma stem cells is regulated by a NOTCH1-SOX2 positive-feedback loop. Nat Neurosci 22:91–105

Wang Q, Hu B, Hu X, Kim H, Squatrito M, Scarpace L, deCarvalho AC, Lyu S, Li P, Li Y et al (2017) Tumor evolution of glioma-intrinsic gene expression subtypes associates with immunological changes in the microenvironment. Cancer Cell 32:42–56.e46

Wang X, Zhou R, Xiong Y, Zhou L, Yan X, Wang M, Li F, Xie C, Zhang Y, Huang Z et al (2021) Sequential fate-switches in stem-like cells drive the tumorigenic trajectory from human neural stem cells to malignant glioma. Cell Res 31:684–702

Wang Z, Sun D, Chen YJ, Xie X, Shi Y, Tabar V, Brennan CW, Bale TA, Jayewickreme CD, Laks DR et al (2020) Cell lineage-based stratification for glioblastoma. Cancer Cell 38:366–379.e368

Weng Q, Wang J, Wang J, He D, Cheng Z, Zhang F, Verma R, Xu L, Dong X, Liao Y et al (2019) Single-cell transcriptomics uncovers glial progenitor diversity and cell fate determinants during development and gliomagenesis. Cell Stem Cell 24:707–723.e708

Wu Y, Fletcher M, Gu Z, Wang Q, Costa B, Bertoni A, Man KH, Schlotter M, Felsberg J, Mangei J et al (2020) Glioblastoma epigenome profiling identifies SOX10 as a master regulator of molecular tumour subtype. Nat Commun 11:6434

Xie XP, Laks DR, Sun D, Ganbold M, Wang Z, Pedraza AM, Bale T, Tabar V, Brennan C, Zhou X et al (2022) Quiescent human glioblastoma cancer stem cells drive tumor initiation, expansion, and recurrence following chemotherapy. Dev Cell 57:32–46.e38

Yabo YA, Niclou SP, Golebiewska A (2022) Cancer cell heterogeneity and plasticity: a paradigm shift in glioblastoma. Neuro Oncol 24:669–682

Yahyanejad S, King H, Iglesias VS, Granton PV, Barbeau LM, van Hoof SJ, Groot AJ, Habets R, Prickaerts J, Chalmers AJ et al (2016) NOTCH blockade combined with radiation therapy and temozolomide prolongs survival of orthotopic glioblastoma. Oncotarget 7:41251–41264

Younes A, Berdeja JG, Patel MR, Flinn I, Gerecitano JF, Neelapu SS, Kelly KR, Copeland AR, Akins A, Clancy MS et al (2016) Safety, tolerability, and preliminary activity of CUDC-907, a first-in-class, oral, dual inhibitor of HDAC and PI3K, in patients with relapsed or refractory lymphoma or multiple myeloma: an open-label, dose-escalation, phase 1 trial. Lancet Oncol 17:622–631

Yu G, Wang LG, Han Y, He QY (2012) clusterProfiler: an R package for comparing biological themes among gene clusters. OMICS 16:284–287

Acknowledgements

The authors thank DKFZ core facilities and the NCT Molecular Precision Oncology Program for excellent technical support for High-Throughput Sequencing, Light Microscopy, Flow Cytometry, Preclinical Research, and Small Animal Imaging. We thank Norman Mack for assisting with animal experiments. This work was supported by the NCT Molecular Precision Oncology Program through project number HIPO016 and by a Shanghai Municipal Education Commission (SMEC) grant to the Shanghai Frontiers Science Center for Biomacromolecules and Precision Medicine at ShanghaiTech University.

Author contributions

Ka-Hou Man: Conceptualization; Validation; Investigation; Visualization; Methodology; Writing—original draft; Writing—review and editing. **Yonghe Wu**: Conceptualization; Validation; Visualization; Methodology; Writing—original draft; Writing—review and editing. **Zhenjiang Gao**: Formal analysis; Validation; Investigation; Writing—original draft; Writing—review and editing. **Anna-Sophie Spreng**: Formal analysis; Validation; Methodology; Writing—review and editing. **Johanna Keding**: Formal analysis; Investigation; Visualization; Writing—original draft; Writing—review and editing. **Jasmin Mangei**: Formal analysis; Investigation; Writing—original draft; Writing—review and editing. **Pavle Boskovic**: Formal analysis; Investigation; Writing—original draft; Writing—review and editing. **Jan-Philipp Mallm**: Formal analysis; Investigation; Writing—original draft; Writing—review and editing. **Hai-Kun Liu**: Writing—original draft; Writing—review and editing. **Charles D Imbusch**: Formal analysis; Investigation; Writing—original draft; Writing—review and editing. **Peter Lichter**: Writing—original draft; Writing—review and editing. **Bernhard Radlwimmer**: Conceptualization; Resources; Supervision; Investigation; Methodology; Writing—original draft; Project administration; Writing—review and editing.

Source data underlying figure panels in this paper may have individual authorship assigned. Where available, figure panel/source data authorship is listed in the following database record: biostudies:S-SCDT-10_1038-S44319-024-00258-8.

Funding

Open Access funding enabled and organized by Projekt DEAL.

Disclosure and competing interests statement

The authors declare no competing interests.

Open Access This article is licensed under a Creative Commons Attribution 4.0 International License, which permits use, sharing, adaptation, distribution and reproduction in any medium or format, as long as you give appropriate credit to the original author(s) and the source, provide a link to the Creative Commons licence, and indicate if changes were made. The images or other third party material in this article are included in the article's Creative Commons licence, unless indicated otherwise in a credit line to the material. If material is not included in the article's Creative Commons licence and your intended use is not permitted by statutory regulation or exceeds the permitted use, you will need to obtain permission directly from the copyright holder. To view a copy of this licence, visit http://creativecommons.org/licenses/by/4.0/. Creative Commons Public Domain Dedication waiver http://creativecommons.org/publicdomain/zero/1.0/ applies to the data associated with this article, unless otherwise stated in a credit line to the data, but does not extend to the graphical or creative elements of illustrations, charts, or figures. This waiver removes legal barriers to the re-use and mining of research data. According to standard scholarly practice, it is recommended to provide appropriate citation and attribution whenever technically possible.

© The Author(s) 2024

Expanded View Figures

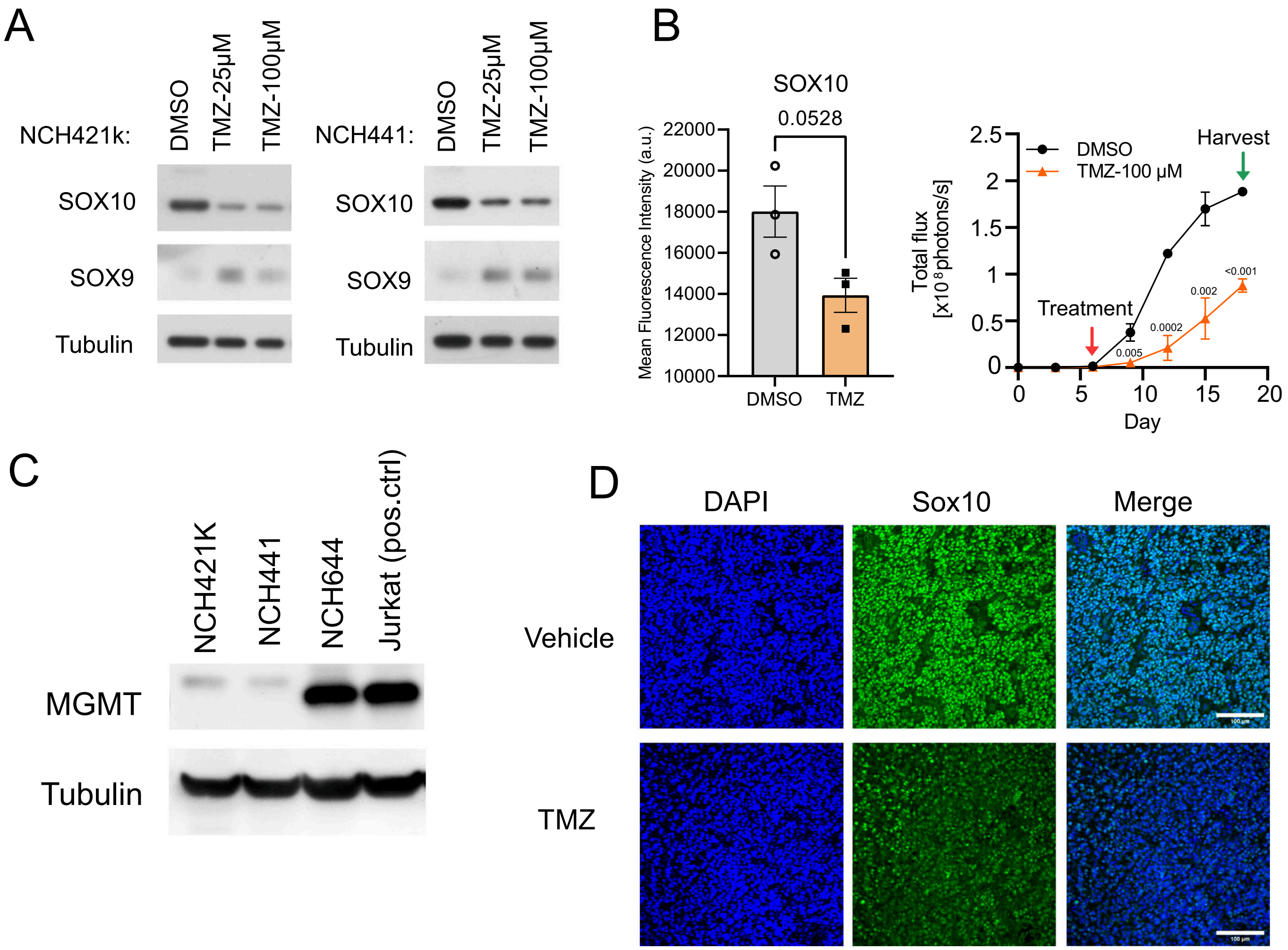

Figure EV1. Temozolomide represses SOX10 expression.

(**A**) Western blot analysis showing short-term (7-day) temozolomide treatment effects on SOX10 and SOX9 expression in NCH421k and NCH441 human glioblastoma cells. (**B**) Temozolomide-induced reduction of *SOX10* expression (left) and cell proliferation (right) of GFP and luciferase dual-labeled NCH644 glioblastoma cells growing in iPSC-derived cerebral organoids. Treatment with DMSO or 100 µM TMZ was started on day 6, and organoids were harvested on day 18. SOX10 expression was analyzed by recording mean fluorescence intensities by flow cytometry on day 18. Cell proliferation was monitored by bioluminescence (photon flux per second) imaging every 3 days. *n* = 3 organoids; mean ± SEM; *P* values were computed with two-tailed unpaired *T* tests. (**C**) Western blot analysis showing MGMT expression levels in SOX10-high glioblastoma stem cells. Protein lysate from Jurkat cells was used as the positive control for MGMT expression. (**D**) Immunofluorescence staining of Sox10 and Sox9 in the vehicle and TMZ-treated mice (Pdgfb/Akt RCAS glioblastoma mouse model) (Rusu et al, 2019). Scale bars = 100 µm. Related to Fig. 1.

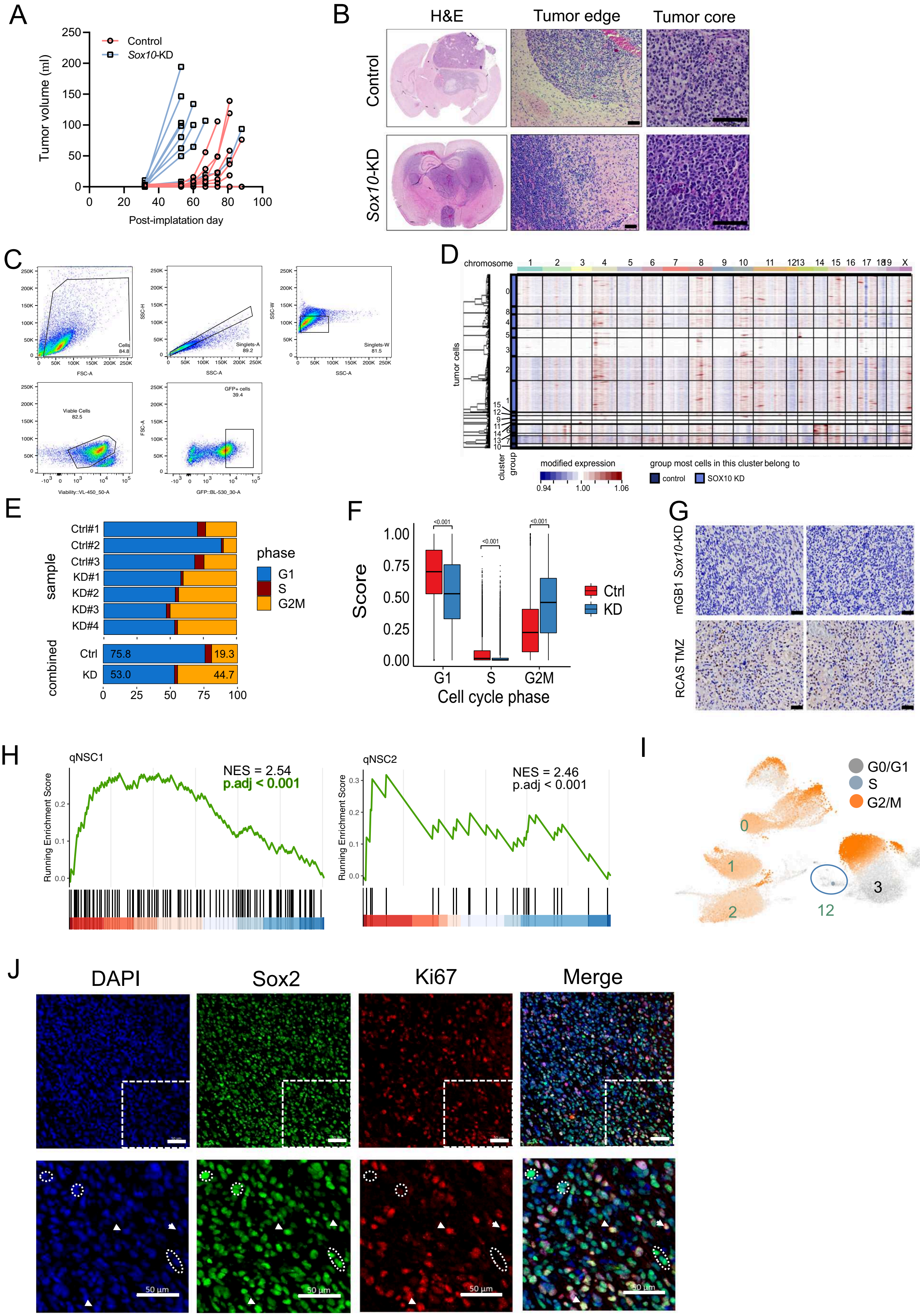
A
Tumor volume (ml)
Post-implatation day
Control
Sox10-KD
0
50
100
150
200
250
0
20
40
60
80
100
B
H&E
Tumor edge
Tumor core
Control
Sox10-KD
C
Cells 84.8
Singlets-A 89.2
Singlets-W 81.5
Viable Cells 82.5
GFP+ cells 39.4
FSC-A
SSC-H
SSC-A
SSC-W
FSC-A
Viability::VL-450_50-A
GFP::BL-530_30-A
D
chromosome
1 2 3 4 5 6 7 8 9 10 11 12 13 14 15 16 17 18 19 X
tumor cells
cluster
group
0 8 4 5 3 2 1 15 12 9 11 6 14 13 7 10
modified expression
0.94
1.00
1.06
group most cells in this cluster belong to
control
SOX10 KD
E
sample
Ctrl#1
Ctrl#2
Ctrl#3
KD#1
KD#2
KD#3
KD#4
combined
Ctrl
KD
75.8
19.3
53.0
44.7
0
25
50
75
100
phase
G1
S
G2M
F
Score
1.00
0.75
0.50
0.25
0.00
<0.001
<0.001
<0.001
G1
S
G2M
Cell cycle phase
Ctrl
KD
G
mGB1 *Sox10*-KD
RCAS TMZ
H
qNSC1
NES = 2.54
p.adj < 0.001
Running Enrichment Score
0.0
0.1
0.2
qNSC2
NES = 2.46
p.adj < 0.001
0.0
0.1
0.2
0.3
I
G0/G1
S
G2/M
0
1
2
3
11
12
J
DAPI
Sox2
Ki67
Merge
50 µm

◀ **Figure EV2. Single-cell RNA sequencing analysis of control and Sox10-KD tumors.**

(**A**) Tumor formation in C57BL6/J mice injected with mGB1 cells expressing non-targeting shRNA (control) and shRNA against Sox10 (*Sox10*-KD) (**B**) H&E staining of coronal brain sections of mice bearing Ctrl and KD tumors. Note that while both tumors resemble grade 4 glioblastoma, *Sox10*-KD tumors have a distinct bi-hemispheric growth pattern, as opposed to the bulky, circumscribed growth observed in the control tumors. Scale bar = 100 µm. (**C**) Gating strategies for isolating GFP-positive tumor cells. (**D**) Analysis of the copy number variations in GFP-positive tumor cells inferred by the R-package infercnv and using GFP-negative cells as reference. Tumor cells are arranged by Seurat clusters (rows) and chromosomes (columns). Copy number gains, red; losses, blue. (**E**) Cell cycle phase distributions of the individual tumors. (**F**) Boxplots showing G1, S and G2/M phase scores in control and *Sox10*-KD tumors. For G1, S and G2M phases, $n = 6747/31090$ cells, 293/1262 cells and 1296/25182 cells from Ctrl and KD tumors, respectively. The box-and-whisker plot shows the interquartile range (box), the median cell cycle scores (line inside the box), and the range of data within 1.5 times the interquartile range from the first and third quartiles (whiskers). *P* values were computed using two-tailed Wilcoxon's rank-sum tests. $^{***}P < 0.001$. (**G**) Immunohistochemistry staining of gamma H2AX (a DNA-damage marker) in KD tumors. TMZ-treated glioblastoma mouse model (bottom) is used as a positive control for the staining. Two fields of view were shown. Scale bars = 50 µm. (**H**) GSEA plot showing the enrichment of qNSC gene signatures (Kalamakis et al, 2019) in cluster 12. Adjusted *P* values (*P*.adj) were calculated using the Benjamini–Hochberg method. (**I**) UMAP visualization of the cell cycle phases of KD tumor cells. Cluster 12 is the qNSC-like cluster. Clusters 0, 1, 2 are the fast-cycling progenitor cell-like tumor cells. Cluster 3 and 11 are the more differentiated tumor cells. (**J**) Immunofluorescence images of co-staining Sox2 (a tumor stem cell marker) and Ki67 (a non-G0/proliferation marker) in KD tumors. The bottom right quadrant of the images were magnified in the bottom panel to highlight the presence of slow-cycling tumor stem cells (Sox2 + /Ki67-, dotted circles) and fast-cycling tumor stem cells (Sox2 + /Ki67 + , arrows). Scale bars = 50 µm. Related to Fig. 2.

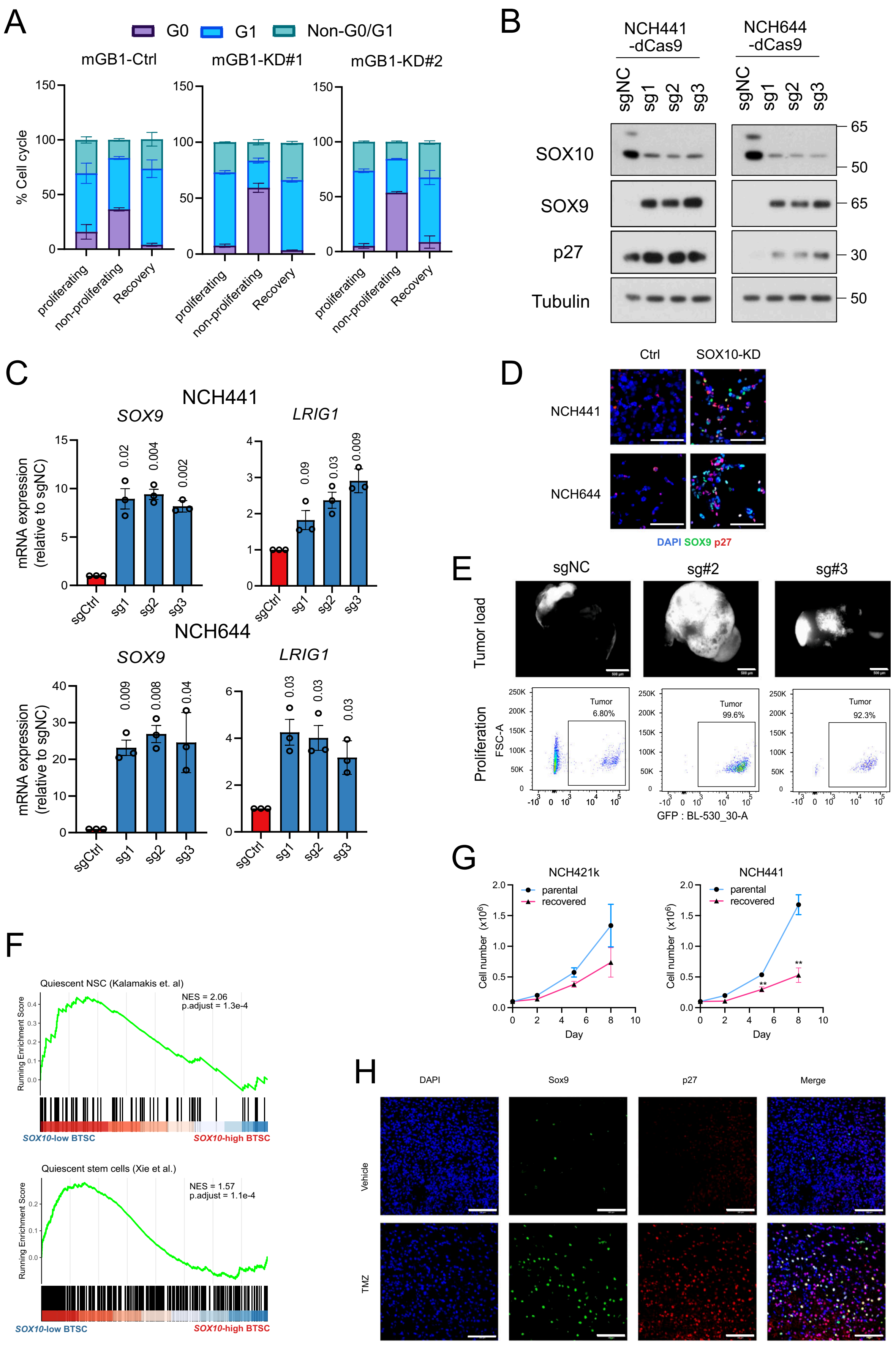
A
G0
G1
Non-G0/G1
mGB1-Ctrl
mGB1-KD#1
mGB1-KD#2
% Cell cycle
150
100
50
0
proliferating
non-proliferating
Recovery
B
NCH441 -dCas9
NCH644 -dCas9
sgNC
sg1
sg2
sg3
SOX10
SOX9
p27
Tubulin
65
50
65
30
50
C
NCH441
SOX9
LRIG1
mRNA expression (relative to sgNC)
0.02
0.004
0.002
0.09
0.03
0.009
sgCtrl
sg1
sg2
sg3
NCH644
SOX9
LRIG1
0.009
0.008
0.04
0.03
0.03
0.03
D
Ctrl
SOX10-KD
NCH441
NCH644
DAPI SOX9 p27
E
sgNC
sg#2
sg#3
Tumor load
Proliferation
FSC-A
Tumor 6.80%
Tumor 99.6%
Tumor 92.3%
250K
200K
150K
100K
50K
0
GFP : BL-530_30-A
G
NCH421k
NCH441
parental
recovered
Cell number (x10^6)
Day
**
**
**
F
Quiescent NSC (Kalamakis et. al)
NES = 2.06
p.adjust = 1.3e-4
Running Enrichment Score
SOX10-low BTSC
SOX10-high BTSC
Quiescent stem cells (Xie et al.)
NES = 1.57
p.adjust = 1.1e-4
H
DAPI
Sox9
p27
Merge
Vehicle
TMZ

◀ **Figure EV3. SOX10 suppression induces quiescent stem cell features.**

(**A**) Bar plots showing the distribution of mGB1 control and *Sox10*-KD cells in the G0, G1 and non-G0/G1 cell cycle phases. Error bars represent mean ± SEM from three independent experiments. (**B**) Western blot showing the upregulation of SOX9 and p27 in control cells (sgNC) and *Sox10*-KD cells (transduced with sg1-3) in SOX10-high NCH441 and NCH644 cells. The molecular weights (in KDa) of the detected proteins are indicated on the right. (**C**) RNA expression of the qNSC markers *SOX9* and *LRIG1*. Mean values ± SEM relative to mGB1 control cells are shown; $N = 3$ biological replicates; P values were calculated with one-sample *T* test. (**D**) Immunofluorescence images of NCH441 and NCH644 control and *SOX10*-KD cells co-stained with *SOX9* and p27. Scale bars = 100 µm. (**E**) GFP-tagged NCH644 control (sgNC) and *SOX10*-KD (sg#2 and sg#3) co-cultured with iPSC-derived cerebral organoids. Stereoscopic fluorescence images showing the growth on day 14 after co-culture. Scale bar = 500 µm. The scatter plots below show the quantification of the tumor load by GFP flow cytometry. (**F**) GSEA plots showing the enrichment of slow-cycling stem cell signatures in SOX10-low vs. SOX10-high BTSCs. Adjusted *P* values (*P*.adj) were calculated using the Benjamini–Hochberg method. (**G**) Growth curves of NCH421k and NCH441 parental cells and cells that have recovered after TMZ treatment. Mean values ± SEM from three experiments are shown. P values were calculated using a two-tailed unpaired *t* test. (**H**) Sox9 and p27 immunofluorescence staining of tumor sections from mice treated with DMSO or TMZ (100 mg/kg, for 5 consecutive days). Scale bars = 100 µm. Related to Fig. 3.

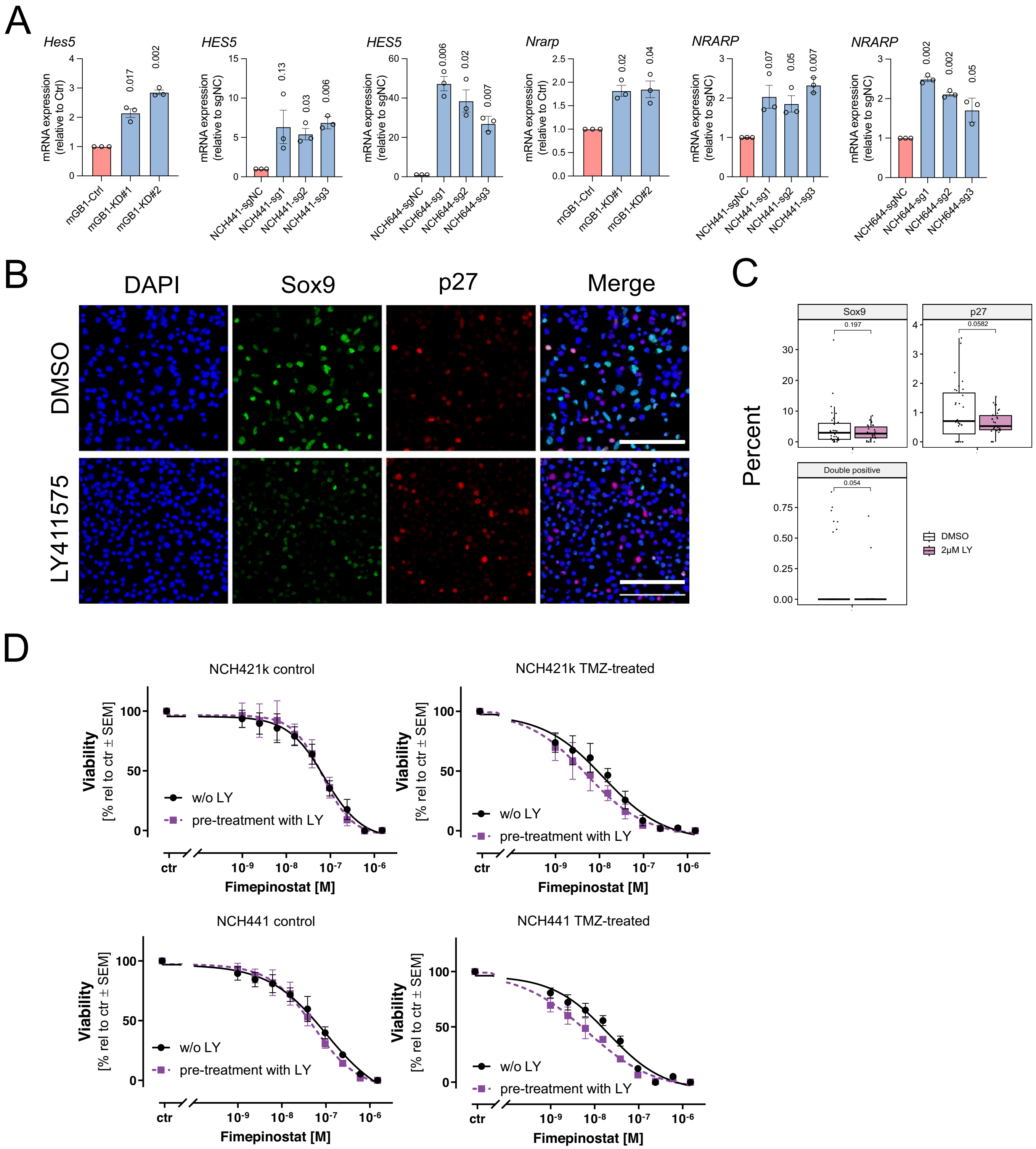
A
Hes5
HES5
HES5
Nrarp
NRARP
NRARP
mRNA expression (relative to Ctrl)
mRNA expression (relative to sgNC)
0.017
0.002
0.13
0.03
0.006
0.006
0.02
0.007
0.02
0.04
0.07
0.05
0.007
0.002
0.002
0.05
mGB1-Ctrl
mGB1-KD#1
mGB1-KD#2
NCH441-sgNC
NCH441-sg1
NCH441-sg2
NCH441-sg3
NCH644-sgNC
NCH644-sg1
NCH644-sg2
NCH644-sg3
B
DAPI
Sox9
p27
Merge
DMSO
LY411575
C
Percent
Sox9
0.197
p27
0.0582
Double positive
0.054
DMSO
2μM LY
D
NCH421k control
NCH421k TMZ-treated
NCH441 control
NCH441 TMZ-treated
Viability [% rel to ctr ± SEM]
w/o LY
pre-treatment with LY
ctr
10^{-9}
10^{-8}
10^{-7}
10^{-6}
Fimepinostat [M]

◀ **Figure EV4. Notch pathway upregulation and inhibition in Sox10-KD cells.**

(**A**) Quantification of relative RNA expression of Notch target genes (*HES5* and *NRARP*) in mouse and human glioblastoma spheroid cultures. Data are represented as mean ± SEM expression levels relative to mGB1 control cells. $n = 3$ biological replicates. *P* values were calculated using one-sample T tests. (**B**) Immunofluorescence images of mGB1 control cells stained with Sox9 and p27. Cells were cultured in reduced growth factor conditions with and without LY411575 treatment. Scale bars = 100 µm. (**C**) Boxplots showing the results of the quantifications of the percentages of Sox9-positive, p27-positive and Sox9 and p27 double-positive cells. Each dot represents the percentage of cells from an image ($n = 30$ images for each condition). The box-and-whisker plot shows the interquartile range (box), the median values (line inside the box), and the range of data within 1.5 times the interquartile range from the first and third quartiles (whiskers). *P* values were computed using two-tailed unpaired T tests. (**D**) Dose-response curves of Fimepinostat alone (black curve) and LY411575 + Fimepinostat (purple curve) in human glioblastoma cells (NCH421k and NCH441) with and without TMZ pre-treatment. Shown are the mean cell viability (%) ± SEM from three technical replicates of one experiment. Related to Fig. 4.

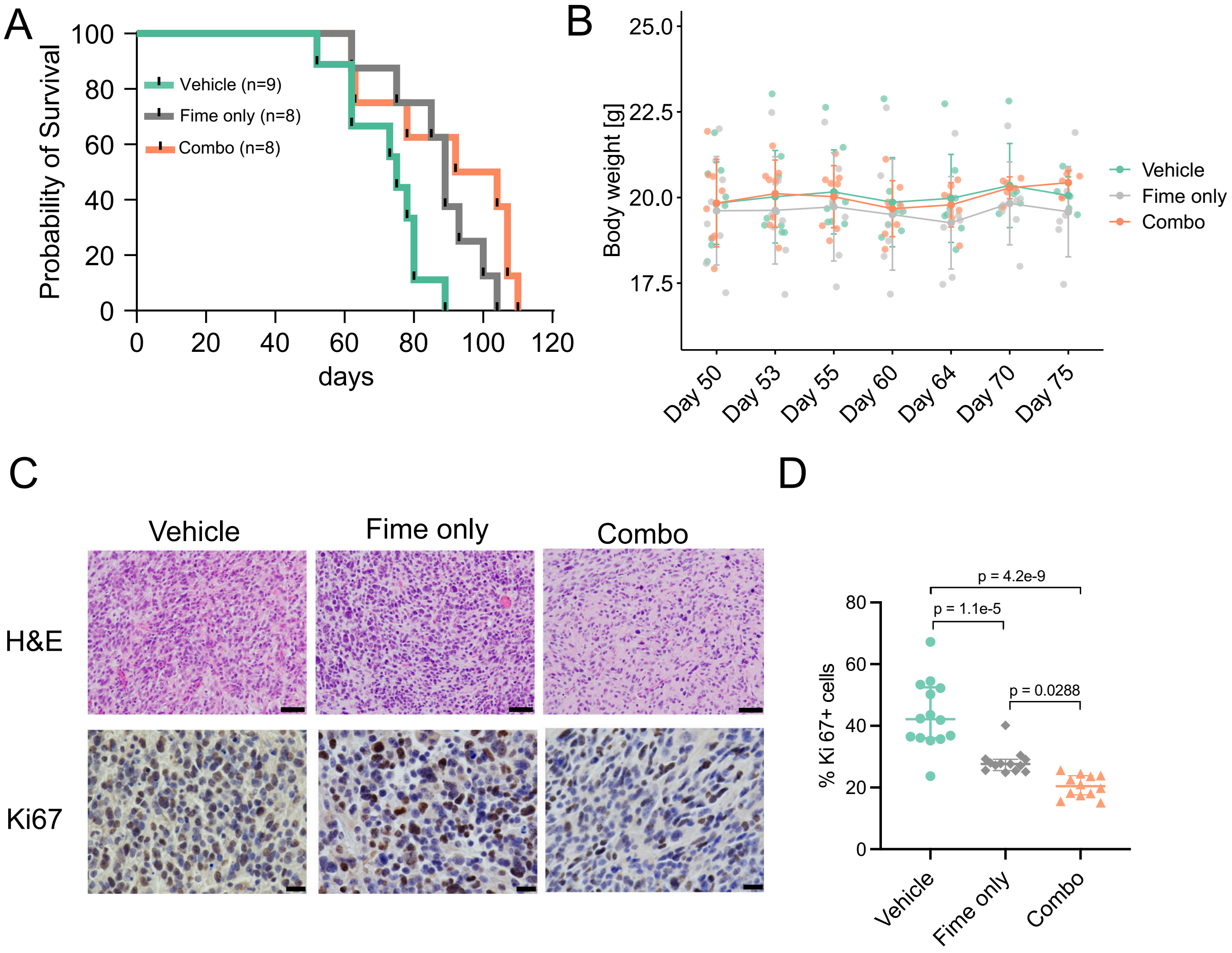

Figure EV5. Fimepinostat treatment of mGB1 tumors in vivo.

(**A**) Kaplan–Meier survival curves of mice intracranially injected with KD cells in Vehicle (*n* = 9), Fime only (*n* = 8) and Combo groups (n = 8), respectively. (**B**) Body weight of animals prior to randomization (Day 50) and during the course of the treatment (Day 53 to Day 75). On day 50, the vehicle group had *n* = 9 animals, the Fime only group had *n* = 8 animals and the Combo group had *n* = 8 animals. Shown are the mean values ± SD. (**C**) H&E (top) and Ki67 staining (bottom) of end-stage tumors of each treatment group. Images of the Vehicle and Combo groups were reused from Fig. 5D. Scale bars for top and bottom panels are 50 µm and 20 µm, respectively. (**D**) Quantification of Ki67 positive cells in (**C**). Shown are the median values ± interquartile ranges. *P* values were calculated with one-way ANOVA with Tukey post-hoc tests to test the level of significance among treatment groups (*n* = 12–13 images from three different animals in each group). Related to Fig. 5.